Applied Clay Science 253 (2024) 107347

Contents lists available at ScienceDirect

Applied Clay Science

journal homepage: www.elsevier.com/locate/clay

Research Paper

μ-Raman spectroscopy as a useful tool for improving knowledge of ancient ceramic manufacturing technologies

Chiara Germinario [a], Giuseppe Cultrone [b], Alberto De Bonis [c,d], Francesco Izzo [c,d], Alessio Langella [c,d], Mariano Mercurio [a,d], Luca Nodari [e], Christopher R. Vyhnal [f], Celestino Grifa [a,d,*]

[a] Department of Science and Technology, University of Sannio, 82100 Benevento, Italy
[b] Department of Mineralogy and Petrology, University of Granada, 18002 Granada, Spain
[c] Department of Earth Sciences, Environment and Resources, University of Naples Federico II, Via Cintia, 80126 Naples, Italy
[d] CRACS, Center for Research on Archaeometry and Conservation Science, Via Cintia 21, 80126 Naples, Italy
[e] Institute of Condensed Matter Chemistry and Technologies for Energy, National Research Council (ICMATE-CNR), I-35127 Padua, Italy
[f] Science Department, The Thacher School, Ojai, CA, USA

ARTICLE INFO

Keywords:
μ-Raman spectroscopy
Archaeological pottery
Ceramic materials
Firing technology
Campania region

ABSTRACT

In recent decades, μ-Raman spectroscopy has become a powerful technique for studying ceramics, with the advantage of performing fast, reproducible and reliable analyses that provide effective information on ceramic technology. In the present paper, the potential of μ-Raman spectroscopy was evaluated by comparing the results of spectroscopic analyses with a wide range of conventional compositional and mineralogical analyses. Particular fragments of pottery from the archaeological site of *Pollena Trocchia* (Campania, Italy), characterized by a variegated color zonation, a symptom of uncontrolled firing conditions, were subjected to in-depth analytical investigation. Data from the μ-Raman measurements were in very good agreement with the analytical set of conventional analyses and permitted to better constrain the firing temperatures, evaluate changes in the oxidative steps, and assert the provenance of volcanic raw materials. The results illuminated that pottery was crafted by mixing a low-CaO base clay with volcanic temper from the environs of Vesuvius and fired in a not well-controlled firing atmosphere, which determined the development of Fe(III) oxides at rims of sherds and Fe (II)-bearing phases at cores. Moreover, even in the absence of newly-formed minerals, firing temperatures were estimated between 900 and 950 °C, as suggested by the mineralogical and spectroscopic evidence of the prograde 10 Å dehydroxylated phyllosilicates.

1. Introduction

Clays have played a key role in human activities since the beginning of human civilizations (Konta, 1995). Due to their abundance on the Earth's surface and their ability to be shaped in different ways and hardened through firing, the use of clays for making pottery and other types of ceramics represents their longest-lasting technological exploitation.

Ceramics are among those archaeological materials that represent a durable example of past material culture. Ceramics provide useful information concerning the chronology of archaeological records, the technological skills achieved by ancient artisans, and the intricate commercial pathways among ancient populations (Tite, 2008).

Analytical instrumentation has advanced in recent decades, from polarized-light microscopes to large synchrotron facilities (Hunt, 2017), and has been utilized to better characterize and understand ancient ceramics. Given these improved analytical capabilities, archaeometric researchers have tried to develop and establish shared analytical protocols for applying useful instrumentation to address complex archaeological and historical questions regarding the sources of raw materials, clay body mixture formulations, firing protocols and pyrotechnology, usage practices, and degradation patterns. However, to adequately address all of these questions, a full investigation of ancient ceramics would necessitate the use of time- and finance-consuming analytical techniques such as optical and scanning electron microscopy, X-ray diffraction spectroscopy, X-ray fluorescence spectroscopy, thermal

* Corresponding author at: Department of Science and Technology, University of Sannio, via De Sanctis snc, 82100 Benevento, Italy.
E-mail address: celestino.grifa@unisannio.it (C. Grifa).

https://doi.org/10.1016/j.clay.2024.107347
Received 20 December 2023; Received in revised form 1 March 2024; Accepted 20 March 2024
Available online 6 April 2024

analysis, Mössbauer spectroscopy, and so on (Hunt, 2017).

More recently, the study of ancient ceramics and other cultural artifacts has shifted to the identification and use of analytical routines that are non-invasive or minimally invasive, thereby preserving the integrity of the artifact and promoting its fast and affordable analytical characterization. Among such methods, μ-Raman spectroscopy (μ-RS) is widely applied in the field of cultural heritage research for the characterization of both organic and inorganic materials, and has found a ready application in the study of paintings and pigments (Bikiaris et al., 2000; Tomasini et al., 2012; Bersani and Lottici, 2016; Caggiani et al., 2016; Germinario et al., 2018b), ceramics (Olivares et al., 2010; Shoval et al., 2011b; Ballirano et al., 2014; De Vito et al., 2014; Medeghini et al., 2014; Cianchetta et al., 2015a; Vandenabeele and Van Pevenage, 2016; Germinario et al., 2018a, 2021; Grifa et al., 2021a), glazes (Ospitali et al., 2005; Colomban et al., 2006; Kirmizi et al., 2019; Alonso-Olazabal et al., 2022), glass (Colomban, 2004, 2008; Baert et al., 2011, 2012; Pinto et al., 2021), lithic fragments (Hernández et al., 2012; Ferrón et al., 2014; Allan and McMillan, 2022), metals (Bouchard and Smith, 2003; Bongiorno et al., 2012; Ospitali et al., 2012; Martina et al., 2013), textiles (Puchowicz and Cieslak, 2022), and organic compounds and residues (Aloise et al., 2014; Short et al., 2015; Retko et al., 2021; Rygula et al., 2021).

μ-RS is a sensitive method for the unambiguous identification of materials in any physical form (crystalline and/or amorphous solids, liquids, gases) since it probes molecular and crystal lattice vibrations. Its non-destructiveness, high spatial and spectral resolution, molecular specificity, portability, applicability to samples of any size and shape make it the most common and effective spectroscopic technique for the study of inorganic solids, providing successful results especially on heterogeneous mixtures on a micrometer scale (Smith and Clark, 2004).

As far as pottery is concerned, μ-RS permits the identification of minerals and their structural characteristics, as well as amorphous and glassy phases based on their molecular vibrational properties. Raman spectra of a well-defined spot in a micrometric range, can detect what is often otherwise undetectable by X-ray powder diffraction (XRPD) analysis (Vandenabeele and Van Pevenage, 2016). Moreover, it offers the opportunity to obtain rapid, replicate measurements of the same spot in the sample.

This non-destructive, molecular fingerprinting technique has the advantage of performing fast, reproducible, and reliable analyses due to its high spatial resolution with no additional, specific sample preparation. Samples prepared for other analyses (for example thin-sectioned samples) can be used with no damage, alteration, or their consumption, thereby minimizing the sample volume needed and better preserving the cultural heritage artifacts under examination (Smith and Clark, 2004; Medeghini et al., 2013; Chiriu et al., 2020).

In addition, the limited invasiveness and small spot size of the laser beam of this micro-analytical technique also permits the investigation of very small areas, and this is particularly effective on heterogeneous ceramic samples since it succeeds in illuminating the potential differences that exist in such complex matrices.

Clues to these heterogeneities could be variations in color of the pottery fragments, both spatially and in cross-section. Some ceramic fragments are characterized by reddish rims and darker (black-to-grey or brownish) cores, which can be due to: a) the presence of unburnt carbon particles within the ceramics that create local reducing conditions, b) the firing of raw clays enriched in organic matter in oxidizing conditions with low heating rates and long soaking times, c) incomplete oxidation within the core due to a short firing time, or d) inadequately controlled firing in reducing conditions and/or quick cooling in oxidizing conditions, hindering the re-oxidation of the entire specimen (Nodari et al., 2004; Maritan et al., 2006; De Bonis et al., 2017a; Oudbashi et al., 2021). In this latter case, the presence of Fe(II)-bearing phases (i.e., magnetite, wüstite, hercynite or maghemite) is promoted due to a high Fe(II)/Fe(III) ratio (Nodari et al., 2004).

On the other hand, a zoned, sandwich-like structure characterized by a red core and dark margins also can be observed in ceramic samples; this feature likely results from firing in an oxidizing environment for most of firing, followed by a later reducing stage (De Bonis et al., 2009). This could be the accidental result of an uncontrolled late firing characterized by the intake of a smoky, reducing atmosphere in the kiln (i.e., from too much wood fuel in the kiln). This condition could have accidentally reproduced an effect similar to that obtained from the process known as the carbon black technique (Jones, 1986; Gardner, 2003; Bonga, 2013).

The potentiality of μ-RS has been evaluated in the present paper. Archaeological ceramic materials with pronounced heterogeneities and color zoning were first investigated by a "traditional" analytical approach using fiber optical reflectance spectroscopy, optical and scanning electron microscopies, hydric tests, mercury intrusion porosimetry, X-ray diffraction, X-ray fluorescence, and Mössbauer spectroscopy, and then by μ-RS, to evaluate its reliability, efficiency, and affordability. The main objective of this research is to highlight the ability of μ-RS to reveal more detailed and comprehensive information on non-homogeneous samples than the more conventional bulk analyses that, due to their intrinsically more destructive and sample-consuming nature, occasionally can be restricted or considered unsuitable.

2. Studied samples

Eight samples of archaeological pottery are the object of this research, namely cooking ware (hereafter CW; pots and a kettle) and tableware (hereafter TW; a bowl and a closed shape) dated back to the end of the 4th century CE (Table 1; Fig. 1).

They were collected from the archaeological site of *Masseria De Carolis* in *Pollena Trocchia*, close to the city of Naples (in the Campania region, southern Italy) in the north-western area of Mt. Somma-Vesuvius (for details on the archaeological site and investigations on other ceramic classes see De Simone et al. (2012), Martucci et al. (2012), Germinario et al. (2021)).

The most relevant feature of the studied samples is the color zoning of the ceramic bodies from rims to cores. They have been divided into two groups based on the type of zoning observed. Samples MDC 38/7, MDC 93/2, and MDC 280/28 (Group 1) show red or reddish-brown rims (average L* = 58.41; a* = 14.99; b* = 22.56) fading to grey cores (average L* = 70.01; a* = 0.93; b* = 6.20) through a tiny intermediate yellow-orange portion (average L* = 68.97; a* = 10.98; b* = 23.03) (Table 1; Fig. 1a).

The other samples have a sharp zonation of ceramic bodies showing two color shades (Group 2): red to reddish brown rims (average L* = 64.74; a* = 15.32; b* = 27.00) and dark grey or brownish grey cores (average L* = 55.50; a* = 2.80; b* = 810.05) (Table 1; Fig. 1b). Only the sample MDC 282/14 showed a reverse zoning, with brownish rims (L* = 62.90; a* = 7.00; b* = 14.37) and a reddish core (L* = 63.38; a* = 25.96; b* = 35.41) (Table 1; Fig. 1b). It should be remarked that measured colors (Table 1) seem lighter likely they appear on the photographs of fresh fractured surfaces (Fig. 1), likely as a result of different lighting conditions.

Ceramic replicas were also selected for comparative μ-Raman analyses. Ceramic test pieces were prepared in the experimental study by De Bonis et al. (2014) with a clayey raw material currently used in the traditional ceramic craft, which was sourced from reworked, weathered, pyroclastic deposits cropping out in the Sorrentine Peninsula in the Campania region of Italy. This raw material is mostly composed of volcanic minerals (feldspar, pyroxene, leucite-bearing scoriae, pumice), along with sedimentary quartz and sandstone. Clay minerals consist of illite/mica and dehydrated halloysite (De Bonis et al., 2013). The specimens of clay were fired at increasing temperatures (from 700 to 1100 °C) to investigate firing dynamics and consequent mineralogical and physical transformations (De Bonis et al., 2014).

Table 1
List of analyzed samples with archaeological information and colorimetric coordinates. Abbreviations: CW: cooking ware; TW: tableware; L*: lightness; a* and b*: chromatic coordinates.

	ID Sample	Ceramic class	Colorimetric coordinates								
			Rim			Intermediate part			Core		
			L*	a*	b*	L*	a*	b*	L*	a*	b*
Group 1	MDC 38/7	CW	64.19	12.16	21.93	65.17	11.52	19.89	73.07	0.59	5.98
	MDC 93/2	CW	59.37	16.96	22.04	72.60	8.41	20.85	71.05	0.81	4.48
	MDC 280/28	TW	51.66	15.86	23.72	69.14	13.02	28.34	65.92	1.38	8.14
Group 2	MDC 84/3	CW	61.24	11.20	22.92	–	–	–	45.71	2.80	12.41
	MDC 84/4	CW	66.68	22.37	33.07	–	–	–	52.57	7.28	14.15
	MDC 84/9	CW	65.66	11.68	25.28	–	–	–	57.62	1.10	9.89
	MDC 282/14	CW	62.90	7.00	14.37	–	–	–	63.24	25.96	35.41
	MDC 429/1	TW	65.38	16.01	26.73	–	–	–	66.08	0.03	3.78

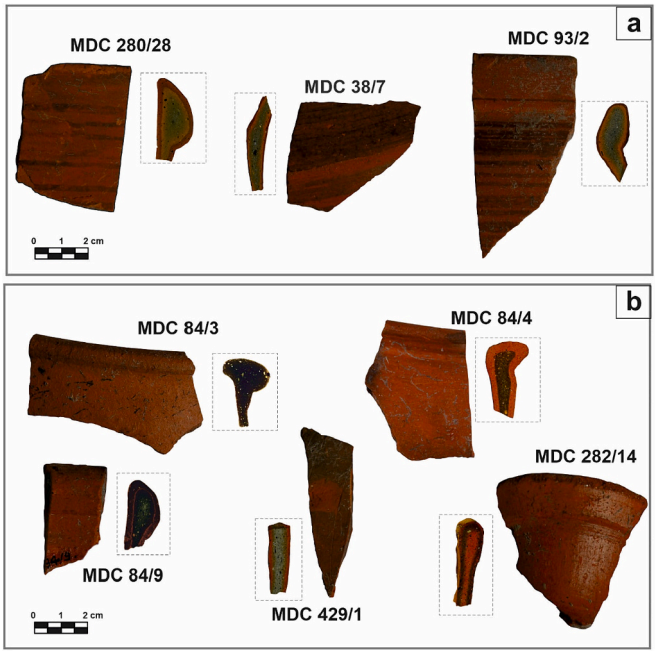

Fig. 1. Archaeological samples and their fresh-fractured surfaces, showing the color zoning of ceramic body of the Group 1 (a) and of the Group 2 samples (b).

3. Analytical techniques

The colors of ceramic bodies were measured using Fiber Optics Reflectance Spectroscopy (FORS). The source consists of a fiber optic cable coupled to a constant current, tungsten-filament, halogen light source (BPS101 - BWTek, Inc.) with a spectral output of 350 to 2600 nm and a Qmini Broadcom grating in the detector. The measuring head geometry was 45°/0°, the analyzed area was 2 mm^2, the spectral range measured was 380–1050 nm, and the data collection time was 0.04 s averaged over 128 scans. The reference was a BWTek inc white plate (99%). The colorimetric coordinates were obtained by setting the primary illuminant D65 and the standard observer CIE 10°. Three measurements per sample were obtained.

Mineralogical and textural features of ceramic pastes were investigated on thin sections via Polarized Light Microscopy (PLM) using a Nikon Eclipse 6400 POL microscope. To accurately distinguish each component of the ceramic bodies (i.e., matrix, a-plastic grains, and pore space), micrographs of a representative area of each sample were taken in both plane- and cross-polarized light. Digital Image Analysis (DIA) was performed on a collage of micrographs using ImageJ software (https://imagej.net/) to assess the Grain Size Distribution (GSD), considering the minimum Feret (mF) value to calculate Krumbein Φ ($\Phi_{mF} = -\log$ (mF)) and the Circularity value (C) to describe the shape of the particles (Grifa et al., 2021b).

The ceramic porosity was evaluated via hydric tests (HyT) on samples weighing more than 10 g, and via mercury intrusion porosimetry (MIP) on samples weighing less than 10 g. Porosity measurements were not obtained on the specimen MDC 429/1 because of the scarce amount of available sample.

Free, forced water absorption and drying tests were carried out on heavy ceramic samples following Normal and RILEM standard procedures (RILEM 1980, 1980; NORMAL 7/81, 1981; NORMAL 29/88, 1988) to determine free water absorption (A_b), forced water absorption (A_f), degree of pores interconnectivity (A_x), open porosity (Po), saturation coefficient (S), drying index (Di), apparent density (ρ_b), and skeletal (real) density (ρ_{sk}). MIP was performed with a Micrometrics AutoPore III 9410 apparatus, exerting a maximum pressure of 414 MPa and measuring pores with dimensions ranging from 0.003 to 360 μm. It allowed for the determination of the open porosity (Po_{MIP}) and the pore size distribution (hereafter PSD).

Mineralogical composition was determined by X-ray Powder Diffraction (XRPD) on powders with grain sizes below 10 μm, obtained using a McCrone micronizing mill (agate cylinders and wet grinding time 15 min). The acquisition of XRPD patterns was carried out by a Philips PW 1730/3710 diffractometer (CuKα radiation, 40 k*V*, 30 mA, curved graphite monochromator, 2θ scanning interval 3–50°, step size = 0.020° 2θ, counting time 5 s per step) equipped with X-Pert data collector software and X-Pert HighScore Plus.

The chemical composition of ceramic bodies, in terms of major (SiO_2, TiO_2, Al_2O_3, Fe_2O_3, MnO, MgO, CaO, Na_2O, K_2O, P_2O_5 in wt%) and trace elements (Rb, Sr, Y, Zr, Nb, Ba, Cr, Ni, Sc, V, La, Ce in ppm), was determined with X-ray Fluorescence (XRF) by using an AXIOS PANalytical Instrument on pressed pellets.

Room Temperature (RT) Mössbauer spectroscopy was performed on a conventional constant-acceleration spectrometer, with a room-temperature Rh matrix 57Co source, nominal strength 1850 MBq. Hyperfine parameters isomer shift (δ), quadrupole splitting (Δ or ε, quadrupole shift when a magnetic coupling is present), half linewidth at half maximum (Γ_+), were expressed in $mm{\cdot}s^{-1}$ while the internal magnetic field (H) in Tesla and the relative area (A) in %. The parameters were

obtained by means of standard least-squares minimization techniques. The spectra, collected on both cores and rims after their mechanical separation, were fitted using a Lorentzian line shape with the minimum number of doublets and sextet. Isomer shift is quoted to α-Fe, using a 4-lines calibration. The samples were prepared by mixing a proper amount of powdered material (50–80 mg) micro-drilled from the different colored portion of the samples with petroleum jelly to avoid the possible particles isoorientation.

Micro-structures were obtained by Scanning Electron Microscopy (SEM) observations on freshly fractured and gold-coated fragments. Energy dispersive spectroscopy (EDS) microanalyses were performed on carbon-coated polished thin sections used for the PLM observation by a Zeiss SEM EVO HD15 equipped with an Oxford Instruments Micro-analysis Unit with Xmax 80 EDS detector. Standard details are reported in Germinario et al. (2019).

On the same thin sections, μ-RS was also undertaken. A JASCO NRS-5100 μ-Raman dispersive spectrometer equipped with a confocal microscope and near-infrared diode laser (785 nm) was used. A collection time of 30, 60 or 90 s, with one to three accumulations and magnification of 100× were adopted. The 521 cm^{-1} peak of a silicon standard was used for the calibration of the laser beam. The acquisition and the elaboration of the Raman spectra, treated by smoothing, was carried out by the Spectra Manager II Software.

4. Results and discussion

4.1. Defining the features of the ceramic bodies

Petrographic observation (PLM) and bulk chemical compositional analyses (XRF) allowed us to recognize the mix-designs of the ceramic bodies and the composition of clay and additional materials (i.e., temper); moreover, the analyses of the pore system (MIP and HyT) returned information concerning the porosity and pore network. These methods provided preliminary information for our subsequent investigation of firing dynamics.

4.1.1. Type of raw materials

4.1.1.1. Cooking wares. CW samples were crafted using a clayey sediment that includes tiny crystals of residual quartz, feldspar, and rare mica (on average $\Phi_{mF} = 5.18$) (Table 2) with the addition of coarser siliciclastic or volcanic grains that, both from a mineralogical and textural point of view, could be considered as tempering additives. Samples MDC 38/7, MDC 93/2 and MDC 84/4 (Fig. 2a-c) were observed to consist of quartz, alkali-feldspar, and siliciclastic arenaceous and silty fragments, along with a minor volcanic component of plagioclase and clinopyroxene plus rare volcanic scoriae (Table 2). GSD ranges from fine silt (0.01 mm) to coarse sand (0.87 mm), with a moderate sorting of particles (average standard deviation (σ) of $\Phi_{mF} = 0.79$) and sub-circular shape (average C = 0.76) (Table 2).

On the other hand, the temper of samples MDC 84/3, MDC 84/9 and MDC 282/14 consists of volcanic phases, namely alkali-feldspar, plagioclase, uncolored and pale green clinopyroxene, garnet, biotite, amphibole, scoriae and pumices (Fig. 2d-f; Table 2). The GSD ranges from fine silt to coarse sand moderately sorted (average $\sigma\Phi = 0.76$). The shape of grains is generally sub-circular (average C = 0.77; Table 2).

Chemical analysis revealed compositions that were generally high in SiO_2 (65.9 to 69.4 wt%), Al_2O_3 (15.6 to 17.1 wt%), and Zr (202 to 275 ppm), and low in Sr (162 to 217 ppm), except for the sample MDC 84/9, which had higher CaO (8.1 wt%) and Sr (290 ppm; Table 3). Despite the varying mineralogy of temper, most of the samples were manufactured with low-CaO clays (LCC, 1.6 to 4.0 wt% CaO; Table 3; Fig. 3). The concentrations of other major and trace elements also vary within a narrow range, except for Ba in sample MDC 84/3, which is significantly higher (692 ppm; Table 3). These compositional features suggest the

Table 2
Mineralogical and textural features of cooking ware and tableware pastes, obtained by PLM and IA. Tableware samples are reported in italics.

	ID Sample	Matrix			Mineralogy					A-plastic grains								GSD (mm)					
		Activity		Texture																Average ϕ_{mF}	$\sigma\phi_{mF}$	Average C
		Core	Rims		Qz	Afs	Pl	Ms	Bt	Cal	Cpx	DRF	Sc	Pum	Amp	Grn	Ol	max	min			
Group 1	MDC 38/7	Inactive	Active	Bimodal	xxxx	xxx	x	tr			tr	x	tr					0.87	0.01	5.0	0.77	0.75
	MDC 93/2	Inactive	Active	Bimodal	xxxx	xxx	x	tr			tr	x	tr					0.70	0.01	4.7	0.81	0.77
	MDC 280/28	Inactive	Active	Bimodal	xxxx	xxx	x	tr		tr	tr	tr	x		tr			0.27	0.01	5.0	0.64	0.77
	MDC 84/3	Inactive	Active	Bimodal	xxx	xx	tr	tr			xx		xx	tr	tr		tr	0.60	0.01	5.0	0.85	0.77
	MDC 84/4	Inactive	Active	Bimodal	xxxx	xxx	x	tr			x	tr	tr					0.40	0.01	5.0	0.67	0.79
Group 2	MDC 84/9	Inactive	Active	Bimodal	xxx	x	tr	tr	tr		xx	x	xx	x	tr	tr		0.60	0.01	5.0	0.82	0.81
	MDC 282/14	Active	Inactive	Bimodal	xxxx	xxx	x	tr	tr		xx	xxx	x					0.66	0.01	4.8	0.72	0.75
	MDC 429/1	Inactive	Active	Bimodal	xxxx	xxx	x	x	tr	xx	–	x	x	tr				0.37	0.01	5.6	0.64	0.77

Legend: Abbreviations according to (Whitney and Evans, 2010)): Qz, quartz; Afs, alkali feldspar Pl, plagioclase; Ms, muscovite; Bt: biotite; Cal, calcite; Cpx, clinopyroxene; DRF, Detrital rock fragments; Sc, scoriae; Pum, pumices; Amp, amphibole; Grn, garnet; Ol: olivine; GSD, Grain Size Distribution; ϕ_{mF}, ϕ minimum Feret; $\sigma\phi_{mF}$, standard deviation of ϕ_{mF} values; C, circularity.; xxxx = predominant, xxx = abundant, xx = frequent, x = sporadic, tr = traces.

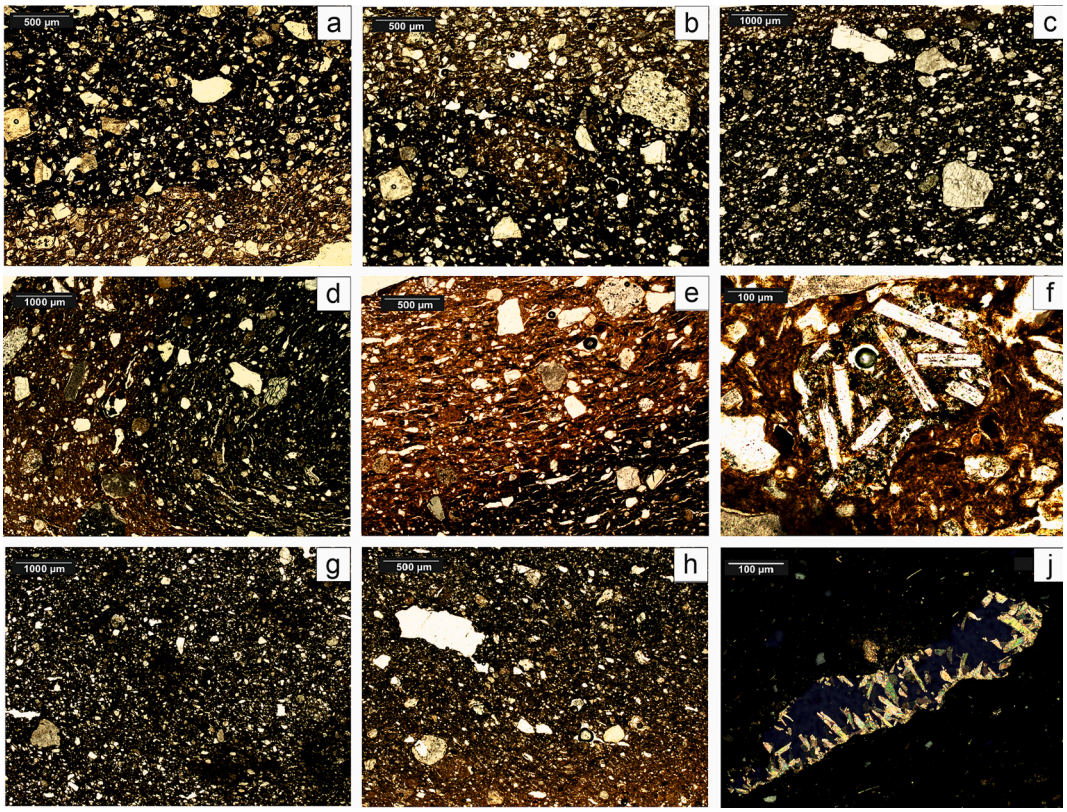

Fig. 2. Micro-photographs of representative ceramic samples. a, b) CW, zoned ceramic body, sample MDC 93/2, 40×, plane-polarized light; c) CW, siliciclastic and (lower) volcanic grains in the ceramic body, sample MDC 38/7, 20×, cross-polarized light; d) CW, ceramic paste containing volcanic temper, sample MDC 84/9, 20×, plane-polarized light; e) CW, zoned ceramic body, sample MDC 84/9, 40×, plane-polarized light; f) CW, volcanic scoria, sample MDC 282/14, 100×, plane-polarized light; g) TW, ceramic body, sample MDC 280/28, 20×, plane-polarized light; h) TW, ceramic body, sample MDC 429/1, 40×, plane-polarized light; j) TW, growth of secondary calcite in pores, sample MDC 429/1, 100×, cross-polarized light.

Table 3
Chemical composition of cooking ware and tableware samples, expressed in terms of major oxides (in wt%, recalculated to 100% on a LOI-free basis) and trace elements (in ppm). Tableware samples are reported in italics.

	Group 1				**Group 2**			
	MDC 38/7	MDC 93/2	*MDC 280/28*	MDC 84/3	MDC 84/4	MDC 84/9	MDC 282/14	*MDC 429/1*
SiO_2	66.0	66.2	63.7	65.9	69.4	62.1	67.1	59.8
TiO_2	0.6	0.6	0.7	0.8	0.6	0.7	0.7	0.9
Al_2O_3	16.1	16.1	16.0	17.2	15.6	15.7	17.1	18.3
Fe_2O_3	5.8	5.8	6.1	7.0	5.4	5.6	6.1	7.3
MnO	0.1	0.1	0.1	0.1	0.0	0.1	0.0	0.2
MgO	2.4	2.3	2.8	2.3	1.8	2.9	2.5	2.8
CaO	4.0	3.8	5.5	2.2	2.1	8.1	1.6	6.2
Na_2O	1.3	1.3	1.2	1.1	1.4	1.0	1.4	0.9
K_2O	3.5	3.5	3.5	3.3	3.4	3.3	3.5	3.5
P_2O_5	0.2	0.2	0.2	0.1	0.1	0.3	0.1	0.2
LOI	1.5	1.3	2.2	0.7	1.1	2.7	1.0	2.5
Rb	191	193	186	230	203	182	303	228
Sr	198	183	260	217	181	290	162	252
Y	48	47	37	44	32	33	37	46
Zr	202	202	222	275	260	189	223	250
Nb	23	23	25	37	30	21	27	37
Ba	451	444	474	691	460	475	489	480
Cr	130	115	112	115	90	114	140	125
Ni	58	58	50	50	28	45	42	54
Sc	14	15	18	16	12	18	16	21
V	107	95	121	143	126	101	145	65
La	42	45	42	57	24	39	46	54
Ce	79	66	79	122	55	64	51	85

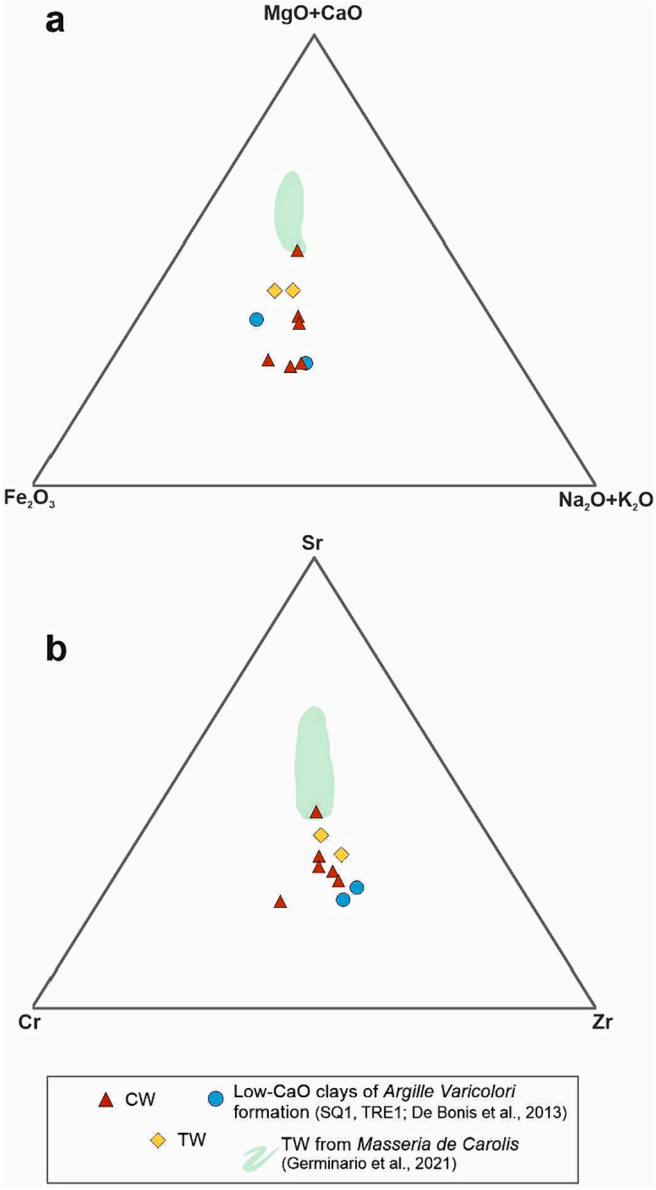

Fig. 3. Triangular diagrams reporting the chemical compositions of the investigated samples (CW and TW) and those from literature, in terms of representative major (a) and trace elements (b), showing the chemical correspondence of low-CaO ceramics with the *Argille Varicolori* formation (samples SQ1 and TRE1, from De Bonis et al. (2013)) and compositional differences with coeval high-CaO tableware (TW) recovered in the same archaeological site (*Masseria de Carolis*) (Germinario et al., 2021).

possible exploitation of a low-CaO clay, as commonly observed for CW in the Campania region and elsewhere (Grifa et al., 2013; Morra et al., 2013; Germinario et al., 2019, 2022; Izzo et al., 2021; Verde et al., 2022), due to good thermal and mechanical properties (i.e., fracture strength, toughness, and thermal shock resistance) of low-CaO ceramic products (Tite et al., 2001; Hein et al., 2009; Muller et al., 2013; Montana, 2017).

4.1.1.2. Tablewares. Samples MDC 280/28 and MDC 429/1 consist of a bowl and a closed shape and, unlike the CW, they have a finer GSD ranging from medium sand (0.37 mm) to fine silt (0.004 mm) (Table 2). Small grains of residual quartz, feldspar and micas are scattered in the isotropic matrix along with less coarse grains of feldspar, clinopyroxene, rare amphibole, siliciclastic rock fragments and juveniles (pumices and scoriae, occasionally containing leucite; Table 2) (Fig. 2g, h). PLM also showed secondary calcite crystallized in the pores of MDC 429/1 (Fig. 2j).

From a compositional point of view, CaO ranges from 5.5 to 6.3 wt%, whereas concentrations of other major and trace elements are comparable with those detected in CW (Fig. 3), unlike what was observed for the other TW unearthed from the same site (*Masseria de Carolis*; Fig. 3) or other TW production from Campania (De Bonis et al., 2016; Germinario et al., 2021; Grifa et al., 2021a; Guarino et al., 2021).

4.1.2. Pore system

Porosity and the pore system of the examined samples were investigated via MIP and HyT. Open porosity (Po) ranged from 20.2 to 30.3% (Table S1). MIP analyses highlighted that the pores fall within a wide dimensional range (0.01 to 2.70 μm) presenting a polymodal PSD (Fig. S1). In particular, PSD curves of Group 1 samples have two main frequency peaks, centred at around 0.14 and 0.55 μm whereas samples of Group 2 showed one main frequency peak, centred between 0.70 and 1.40 μm (Fig. S1).

The low interconnectivity of the porosity (A_x) (7.4 to 10.5%) was highlighted by the high inclination of the absorption curve in the section between the free and the forced absorption (Fig. S1). It could be related to a tortuous pore system due to an advanced sintering stage, as also demonstrated by the high values of apparent density ρ_a ranging from 1.74 to 1.96 g/cm^3 (Table S1).

4.2. Comparative analyses

The following sections provide a comparison between μ-RS and other bulk and micro-analytical conventional techniques commonly used to assess the ceramic technology for compositional and mineralogical features of a-plastic grains and the ceramic matrix. Specifically, three key factors were evaluated: i) the provenance of the temper, ii) the Equivalent Firing Temperatures (EFTs), which consider mineralogical and microstructural transformations occurring in clays upon firing, and depend not only on maximum firing temperature, but also on firing time and redox conditions in the kiln atmosphere (De Bonis et al., 2017b), iii) the redox conditions, which ultimately determine the color of the ceramic bodies.

4.2.1. Defining the provenance of the temper: μ-RS vs EDS microprobe analyses

Energy Dispersive Spectroscopy (EDS) is a valuable technique that allows for the determination of the chemical composition of both crystalline and amorphous species used as temper in ceramics, supporting the PLM observations.

EDS microanalyses revealed that the alkali-feldspars are K-feldspar ($An_0Ab_{6\text{-}25}Or_{75\text{–}94}$), whereas plagioclase composition ranges from $An_{57}Ab_{38}Or_5$ to $An_4Ab_{93}Or_3$ (Table S2). Uncolored and pale green clinopyroxene is diopside (MgO = 9.3 to 17.7%; FeO = 3.4 to 12.4%) (Morimoto, 1988) (Fig. 4, Table S3). Garnet crystals are primarily andradite (50 mol%) (Locock, 2008) and olivine has composition of Fo_{87} (Table S4). OH-bearing phases are also present, and include biotite (Mg# 0.21–0.51) and calcic amphibole (hastingsite) (Table S4). Fe-oxides, Ti-oxides, and ilmenite only occur as accessory phases (Table S4), and leucite was occasionally observed in scoriae (Table S4).

Considering the effectiveness of the μ-RS in the identification of mineral phases including their polymorphs and solid solution end-members (Medeghini et al., 2014), the results of micro-chemical analyses (Fig. 4a) have been correlated to vibrational frequencies of temper grains by μ-RS measurements. Feldspar is readily recognized by the presence of the two most important Raman peaks lying between 450 and 515 cm^{-1} (Fig. 4b), assigned to the ring-breathing modes of the four membered rings of SiO_4 tetrahedra (Fintor and Gyalai, 2012). The most intense peak occurs within the 507–515 cm^{-1} range (peak I_a), attributed to a mixed Si–O–Si/Si–O–Al bending/stretching mode, along with a

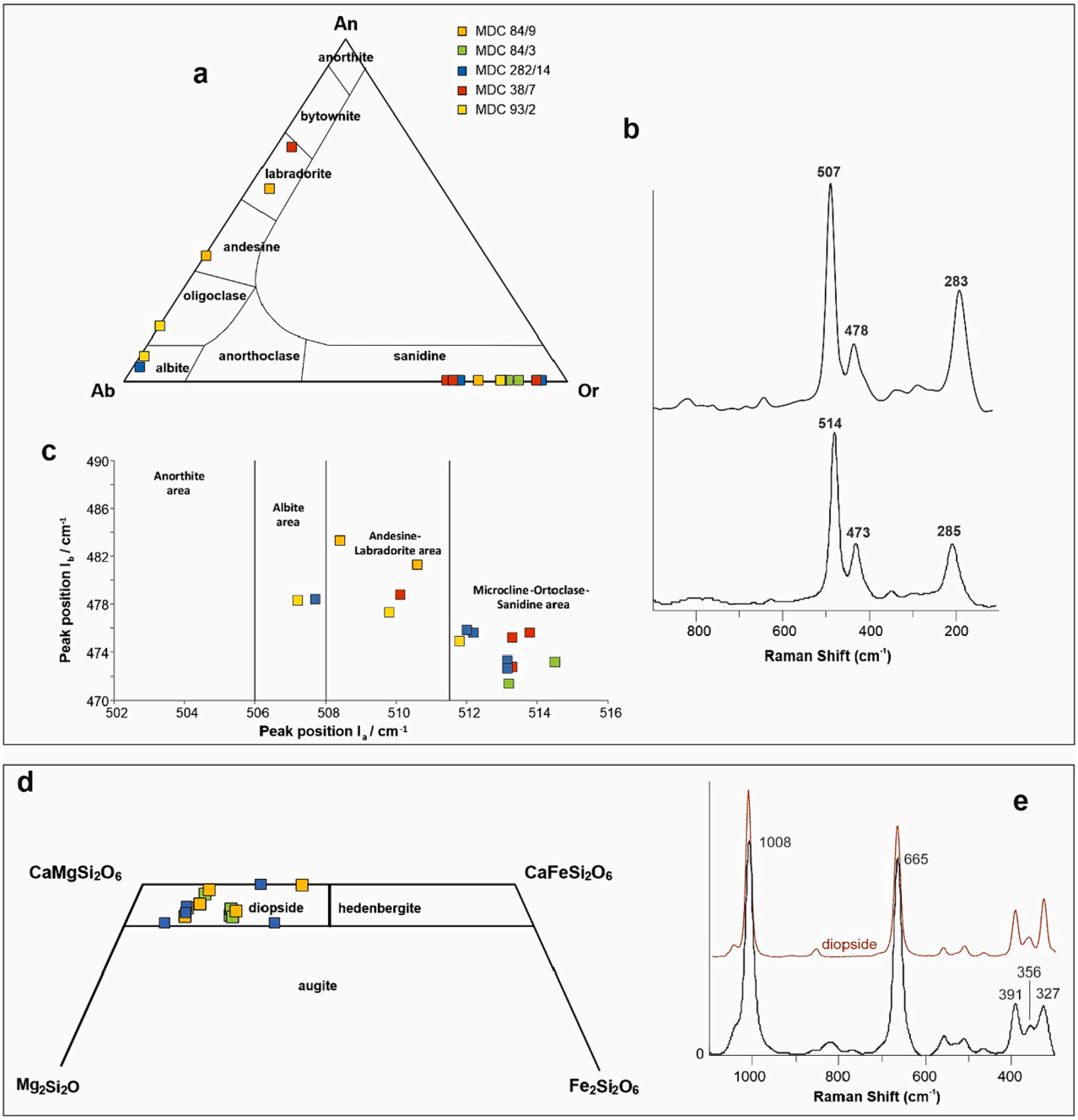

Fig. 4. Diagram showing the compositional data of feldspars obtained via EDS (a), the Raman spectra of the feldspars (b) and discrimination diagrams of feldspar grains based on the positions of the most important bands (I_a: 502–516 cm^{-1} and I_b: 470–490 cm^{-1}) (c). Classification diagrams based on the mineral chemistry of pyroxenes (d) showing that all analyzed crystals have the composition of diopside, as confirmed by Raman spectra (e) (the reference spectrum of diopside (RRUFF standard X050060) was reported in red). (For interpretation of the references to color in this figure legend, the reader is referred to the web version of this article.)

weaker peak at 470–490 cm^{-1} (peak I_b).

A criterion to effectively classify feldspars is based on the position of these peaks within the above reported range, based on the changes in their vibrational frequencies as a function of feldspar composition (Fintor and Gyalai, 2012). In the classification diagram (Fintor and Gyalai, 2012) alkali-feldspar is characterized by higher frequencies of the I_a peak (Fig. 4c), in agreement with EDS data (Table S1), and plagioclases are clustered in the andesine-labradorite and albite areas (Fig. 4c).

Likewise, the pyroxene group is also amenable to reliable identification and characterization via μ-RS, since in crystalline materials spectral patterns and shifts in peak positions are a consequence of the variations in chemical composition (Wang et al., 2001). In particular, systematic peak shifts of Raman active modes as a function of Fe content turned out to be an index for an estimation of the major-element composition (Mg, Fe, Ca) of pyroxenes (Huang et al., 2000). Pyroxenes generally exhibit a Si—O stretching mode above 800 cm^{-1}, Si—O bending modes between 500 and 800 cm^{-1} and SiO_4 rotation and metal–oxygen modes below 500 cm^{-1} (Huang et al., 2000). In agreement with EDS data (Fig. 4d; Table S3), the wavenumber positions of the three modes at ca. 325, 356 and 390 cm^{-1} in the temper grains of the studied samples (Fig. 4e) are very close to the values given for the diopside (Huang et al., 2000; Wang et al., 2001) (Fig. 4e).

The Raman spectra of the other phases are also consistent with

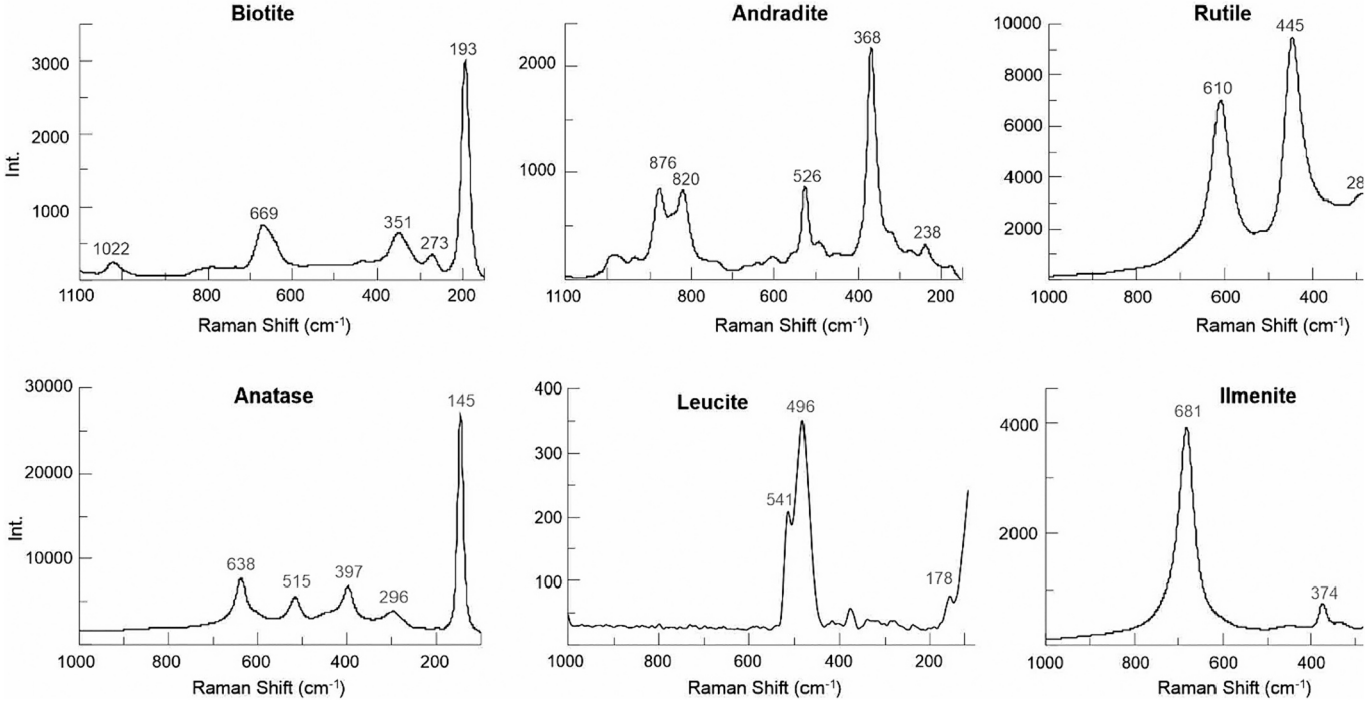

Fig. 5. Raman spectra of some accessory mineralogical phases detected in the ceramic bodies.

micro-chemical data: the mica displays spectral lines consistent with biotite (ca. 193, 273, 350, 670, 1022 cm^{-1}) (Singha and Singh, 2016); garnet has the spectral features of andradite (368, 525, 820, 875 cm^{-1}) (Fig. 5) (Kolesov and Geiger, 1998), and the amphibole spectrum is comparable to that of hastingsite (185, 290, 378, 534, 750 cm^{-1}) (RRUFF standard R070124) (Lafuente et al., 2015). Typical peaks of forsterite (820, 851 cm^{-1}) and leucite (178, 496, 527 cm^{-1}) were also measured (Fig. 5).

The correlation between EDS and Raman microanalyses leads us to hypothesize that the volcanic-bearing cooking wares were produced in the Vesuvius environs due to the consistency of the temper minerals with the rock-forming minerals of Somma-Vesuvius volcanic products (Santacroce et al., 2008; Morra et al., 2013; Redi et al., 2017). However, as verified for other coeval ceramic productions (Germinario et al., 2018a, 2021), the mixed source of volcanics and siliciclastic grains could also be derived from a select deposit, likely an alluvial sand, that mixed together Apennine sandy-like materials along with volcanics from the Vesuvius environs.

μ-RS has the added advantage of being able to obtain reliable mineral data on ceramic matrix at the sub-micrometric scale-spot sizes. High magnification (100×) by μ-RS, in fact, allows for the detection of excitation bands in other accessory phases such as Ti- and Fe-oxides, which would otherwise be recognized only as bright particles scattered in the amorphous phase of clay matrix via SEM-EDS. μm-scale rutile (ca. 145, 284, 455, 610 cm^{-1}) and anatase (ca. 143, 295, 395, 515, 638 cm^{-1}) were observed (Fig. 5) (Fintor and Gyalai, 2012), along with hematite (ca. 225, 290, 410, 608 cm^{-1}) (Zoppi et al., 2008) and magnetite (ca. 304, 540, 670 cm^{-1}) (Shebanova and Lazor, 2003). In sample MDC 282/14, the hematite spectrum shows an additional band at ca. 665 cm^{-1}, which could represent a common and natural transformation process of Fe_2O_3 to Fe_3O_4 (Lofrumento et al., 2004) or the effect of Al-for-Fe substitution in the hematite structure (Zoppi et al., 2008). Moreover, ilmenite (225, 374, 681 cm^{-1}) (Wang et al., 2004) has also been detected in the ceramic matrix (Fig. 5).

4.2.2. *Defining EFTs: μ-RS vs XRPD and SEM analyses*

A ceramic body can be considered to be a man-made metamorphic rock, containing residual minerals (clays and siliciclastic fragments) from the precursor sedimentary materials, together with newly-formed crystalline, amorphous, and low-ordered phases formed during firing in a kiln (Bersani et al., 2016). The varied nature of the mineralogical phases present in fired ceramics make them a complex object to study, particularly when attempting to reconstruct the firing temperatures and kiln atmospheric conditions during their production process.

The most commonly used technique for the determination of EFTs is X-ray powder diffraction, which can identify those micro- and cryptocrystalline phases that often represent important markers for firing conditions. XRPD, if coupled with SEM observations on the freshly fractured surfaces of samples, can provide useful insights in the evaluation of the sintering and vitrification stage of the clayey matrix (Maniatis and Tite, 1981).

XRPD bulk analysis on the investigated samples revealed the ubiquitous presence of quartz and feldspar as the main a-plastic grains along with traces of illite/mica (Fig. 6; Table 4).

The intensity of phases with an approximately 10 Å basal distance (illite/mica) (Mercurio et al., 2016) can be considered as a useful thermal marker in pottery made with LCC. Experimental data suggest the total breakdown of these phases and the consequent disappearance of the aforementioned peak over 950 °C (Jordán et al., 1999; Cultrone et al., 2001; Grifa et al., 2009). In our samples, the 10 Å dehydroxylated illite-like phases can be still observed, although the diffraction peak appears with different intensities (Fig. 6), suggesting that EFT did not exceed 950 °C.

EFTs are broadly confirmed by vitrification structures observed via SEM; the samples show: a) continuous vitrification structures with fine bloating pores in the cores of samples (following the nomenclature by Maniatis and Tite, 1981) (Fig. 7a, b), and b) extensive vitrification structures at the rims of the ceramics, with parallel-oriented clay flakes welded to form continuous smooth-surface areas with pores following the shape of smoothed surfaces (Fig. 7c, d).

The continuous vitrification structures in the core and the extensive vitrification structures at the rims are consistent with data from the literature (Maniatis and Tite, 1981), which reports that these structures developed from 850 and 950 °C in reducing and oxidizing conditions,

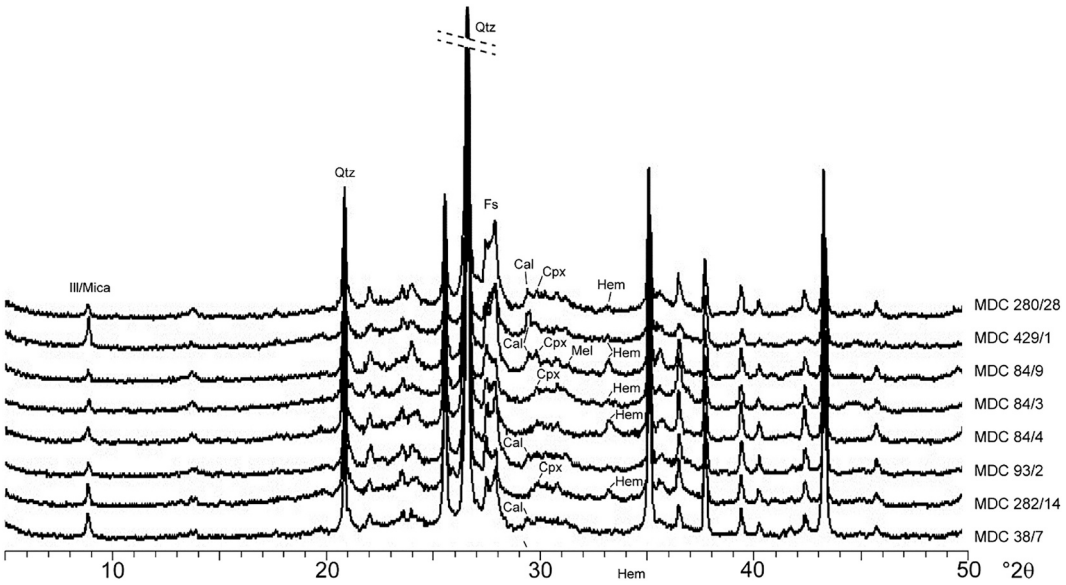

Fig. 6. XRPD patterns of CW. Abbreviations: Qtz, quartz; Fs, feldspar; Cal, calcite; Cpx, clinopyroxene; Mel, melilite; Hem, hematite; Ill/Mica, illite/mica.

Table 4
Mineralogical composition of cooking ware and tableware samples (obtained via XRPD). Tableware samples are reported in italics. Legend: xxxx = predominant, xx = frequent, x = sporadic, tr = traces.

Group	ID Sample	Quartz	Feldspar	Illite/mica	Calcite	Clinopyroxene	Melilite	Hematite
Group 1	MDC 38/7	xxxx	xx	tr	tr	–	–	–
	MDC 93/2	xxxx	xx	tr	tr	–	–	–
	MDC 280/28	xxxx	xx	tr	tr	x	–	tr
Group 2	MDC 84/3	xxxx	x	tr	–	tr	–	tr
	MDC 84/4	xxxx	x	tr	–	–	–	tr
	MDC 84/9	xxxx	xx	tr	tr	tr	tr	x
	MDC 429/1	xxxx	xx	xx	x			x
	MDC 282/14	xxxx	x	tr	–	tr	–	tr

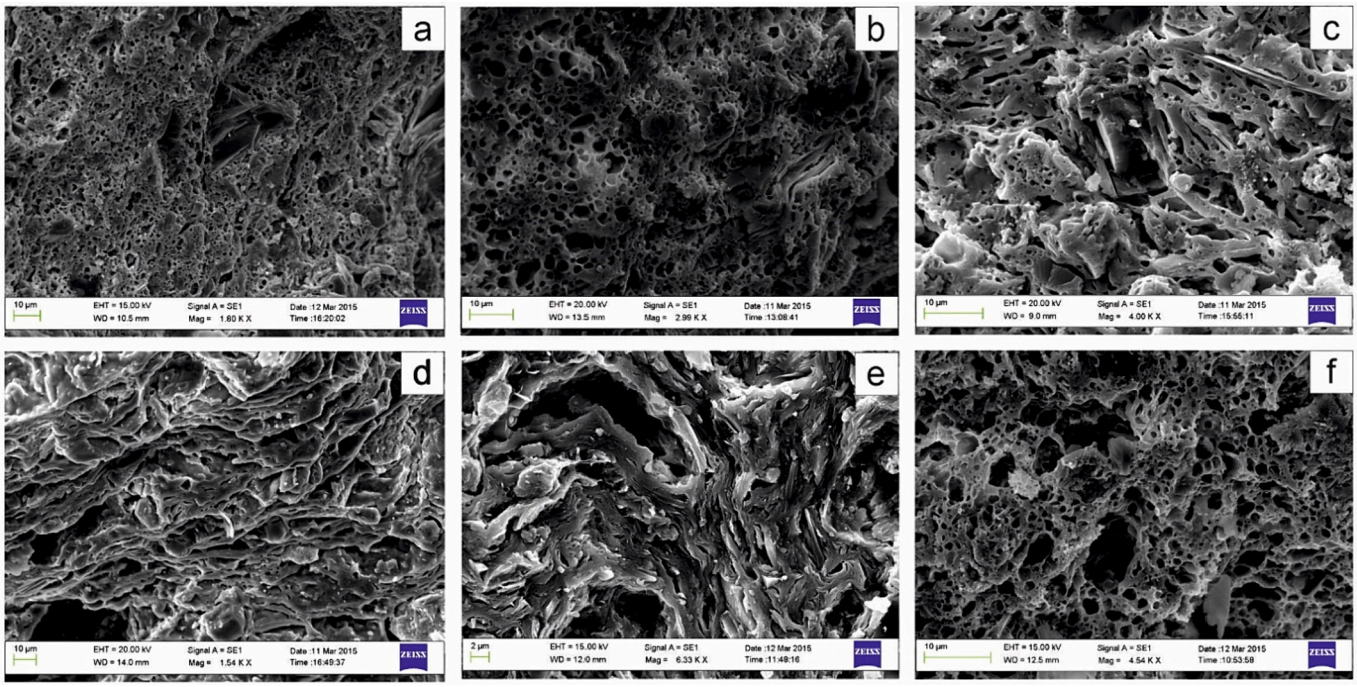

Fig. 7. Micro-textural images of CW samples. a) MDC 93/2, continuous vitrification structure with fine bloating pores; b) MDC 93/2, matrix of the core with deformed mica crystal; c) MDC 280/28, matrix at rim of sample; d) MDC 84/3, extensive vitrification structure at rims of sample; e) MDC 84/9, matrix at rim of sample; f) MDC 84/9, matrix at core of sample showing continuous vitrification structure with fine bloating pores.

respectively. Therefore, this conclusion supported the diffractometric data.

It should be noted that the mineral assemblage of sample MDC 84/9 is quite different from the other investigated CW due to its higher CaO content, which resulted in the formation of newly-formed Ca-silicates, namely melilite and clinopyroxene (Fig. 6; Table 4), which are confirmed by the compositional data obtained by EDS analysis of the reaction rims (Fig. S2). The coexistence of newly-formed phases together with residual calcite, which survived thermal decomposition, suggests firing temperatures of 900–950 °C (Cultrone et al., 2001; Grifa et al., 2009; De Bonis et al., 2014). Regarding the vitrification structures, the rims show wavy strips of glass due to the melting of phyllosilicates edges (Maniatis, 2009), whereas the core displays a continuous vitrification structure with fine bloating pores (Fig. 7f), confirming that firing

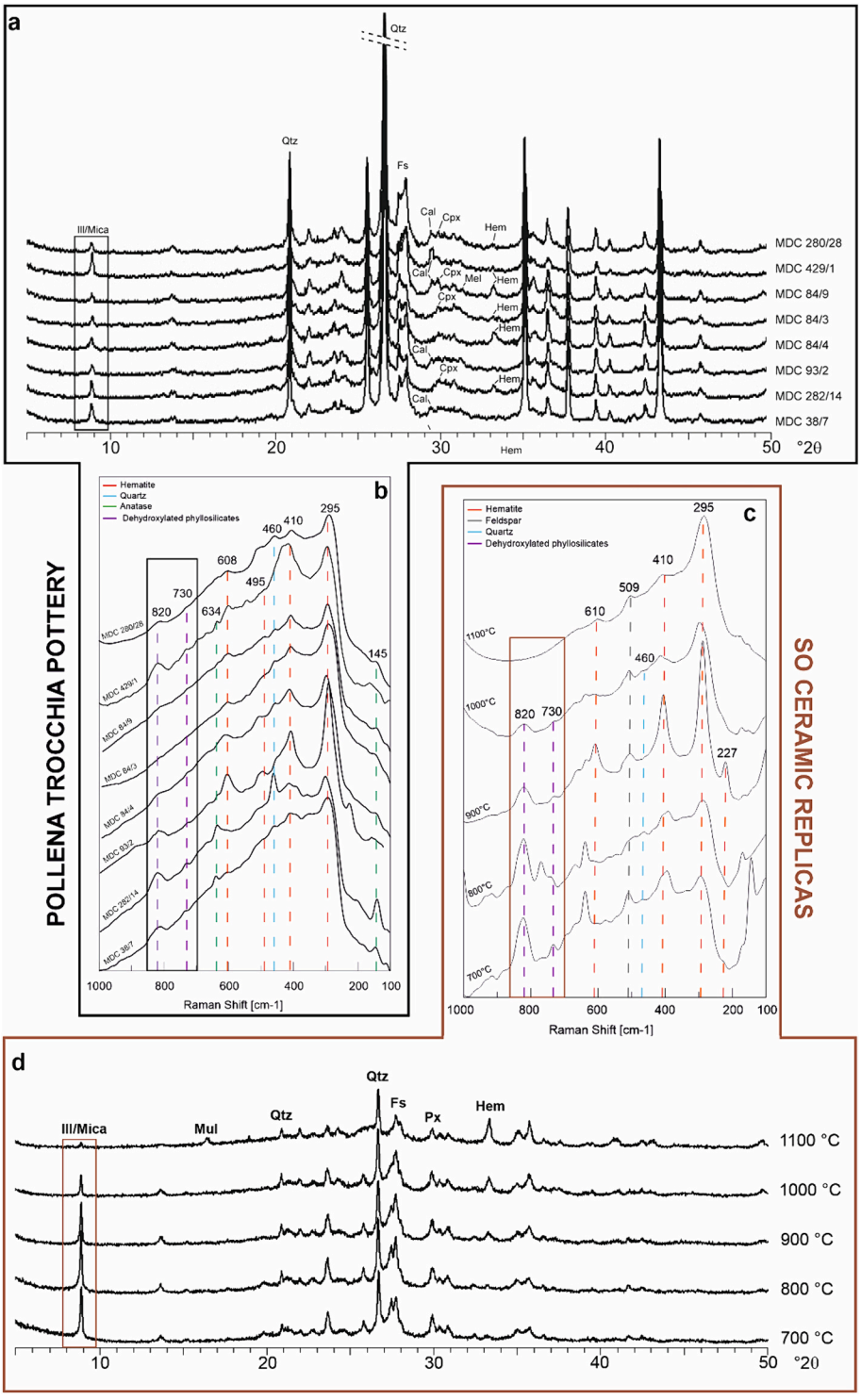

Fig. 8. XRPD patterns of CW (a) the peaks of 10 Å illite-like phases compared with b) Raman spectra of the same samples, in which peaks at ca. 730 and 820 cm^{-1} decrease, consistent with XRPD data. c) Raman spectra of ceramic replicas made with Campanian LCC from the Sorrento peninsula (SO ceramic replicas), in which the same spectral features are evident, testifying to the progressive breakdown of illite-like phases; d) XRPD patterns of ceramic replicas (details and mineral abbreviations are from De Bonis et al. (2014).

temperatures were not well-controlled.

XRPD bulk analyses only detected hematite and not any reduced iron phases (Table 4) which suggests firing under oxidizing conditions. However, the expected dominant red hue (Nodari et al., 2007) is not observed as the samples are characterized by an obvious color zoning featured by the black core. Actually, more specific analyses, including μ-RS and Mössbauer spectroscopy, are needed to better understand the firing dynamics, to detect mineralogical changes due to thermal gradients that resulted from an inhomogeneous temperature distribution in the pottery, and to evaluate the oxygen fugacity in the furnace.

In an effort to provide an additional way to estimate the firing temperatures of ceramic matrices, we obtained Raman spectra from newly-formed and residual mineralogical phases. Applications of μ-RS for this purpose are often based on distinguishing between various TiO_2 polymorphs, which may transform during the heating process of clayey materials. These TiO_2 polymorphs may be used as thermal markers to estimate the firing temperature as anatase tends to convert into rutile above 900 °C (Bouzidi et al., 2013). Therefore, the coexistence of both polymorphs in our samples suggests that the firing temperature was near the temperature of the TiO_2 polymorph's transformation (ca. 900 °C) (Gennari and Pasquevich, 1999), consistent with EFTs estimated via XRPD and SEM. However, the role of titanium oxide phases as thermal markers is controversial, as several investigations have revealed that different conditions may interfere with the temperature of the phase transition. Variations in particles size and the presence of Fe_2O_3 can reduce the transition temperature by around 100 °C and accelerate the phase transformation (Gennari and Pasquevich, 1999), whereas anatase contained in kaolinites generally converts to rutile above 1100 °C (Shoval et al., 2011a).

Thus, we focused our attention on acquiring Raman spectra of ceramic matrices from different positions in our samples, for a comparison with XRPD patterns.

μ-RS measurements revealed spectral features consistent with XRPD data, particularly with the intensity of diffraction peaks of residual, dehydroxylated clayey minerals (Fig. 8a). In the investigated areas, bands of hematite, quartz, and anatase are present along with some broad and weak bands at ca. 730 and 820 cm^{-1}. As reported in the literature (Legodi and de Waal, 2007; Shoval et al., 2011a), these peaks represent dehydroxylated clays, in which the framework of clay minerals is completely distorted by the removal of structurally bonded hydroxyls, with the consequent formation of short-range ordered phases (Shoval et al., 2011b), resulting in broader and weaker Raman bands. Interestingly, the progressive reduction of the intensity of Raman band (Fig. 8b) is consistent with what was observed with the 10 Å diffraction peak as a function of increasing EFTs.

To further confirm this evidence, μ-Raman analyses were performed on thin-section of ceramic replicas made with low-CaO Campanian clays (SO ceramics) and fired at increasing temperatures from 700 to 1100 °C (De Bonis et al., 2014). The XRPD and μ-RS spectra obtained from our archaeological pottery samples (Fig. 8a, b) are consistent with those obtained from the matrices of the ceramic replicas (8c, d), which also show bands at ca. 730 and 820 cm^{-1} that decrease in intensity and gradually become broader as the firing temperature increases until they completely disappear at 1100 °C. Thus, the detection of these bands in the Raman spectra definitively indicates the presence of residual dehydroxylated phases which constrain the firing temperature.

4.2.3. *Defining the redox conditions: μ-RS vs Mössbauer spectral analyses*

The zoned ceramic body of the investigated pottery suggests a variability in temperatures and/or oxygen fugacity during the firing and cooling stages and that the changes in color could be due to different redox conditions. XRPD analyses, however, were unable to explain the color zoning as reflecting differences in mineralogy (the only iron oxide that was observed in the XRPD spectra was hematite).

Mössbauer spectroscopy performed on both cores and rims of the zoned fragments provided some clarification of the firing dynamics. In general, the main difference between zoned ceramic cores and margins is in the relative amount of Fe(II) contained. Cores show a higher Fe(II) content, indicating the presence of a local, non-oxidizing environment during firing, whereas Fe(III) oxide, in variable amounts, is mainly found in the external margins of the pottery along with other ferric and ferrous species. The presence of Fe in both oxidation states is typical of a poorly controlled firing atmosphere.

As far as the rims of the ceramics are concerned, all Mössbauer spectra showed an intense central absorption, attributable to paramagnetic ferric iron sites, together with a broad magnetic pattern, due to the presence of iron oxides. The best model fits of the paramagnetic absorption were obtained by using only one component, whose hyperfine parameters are compatible with those of Fe(III) in octahedral coordination, namely the hematite (Table S4). The large linewidth suggests the superposition of Fe(III) sites, probably due to the presence of paramagnetic and superparamagnetic components (Fig. 9a). Superparamagnetic contribution arises from the presence of nanosized ferric oxides, that, in an RT Mössbauer spectrum, shows a doublet instead of the sextet, typical of magnetically coupled species. In sufficiently small nanoparticles, magnetization can randomly flip direction under the influence of temperature, and the related Mossbauer spectrum exhibits a doublet, as in a paramagnetic regime. The low value of the magnetic hyperfine field (ca. 49–50 T instead of 51.7 T) in the pure, macrocrystalline hematite can be due to substitution of Fe (III) by Al (III) in the hematite and/or to the low crystallinity of the oxide (Nodari et al., 2004, 2007).

In contrast to the general trend, the brown rims of sample MDC 282/14 present a magnetic absorption that can be fit by using two different sextets whose parameters are close to those of magnetite (Fig. 9b).

On the other hand, the spectra collected on the cores show a high Fe (II) content, 60–90% distributed over tetrahedral and octahedral sites (Fig. 9c). The presence of Fe(II) in tetrahedral sites is attributed to the presence of Fe(II) bearing spinels, such as hercynite and suggests a non-oxidizing environment with a low oxygen fugacity, fO_2.

Data obtained via μ-RS on cores, rims, and intermediate parts orange in color seem to confirm such a hypothesis. Despite the low Raman scattering effects of the ceramic matrix components and fluorescence commonly associated with these types of samples, μ-RS on red rims detected hematite, as indicated by the bands at ca. 225, 292, 410, 498 and 606 cm^{-1} (Fig. 9d).

On the orange matrix of Group 1 samples (MDC 93/2, MDC 38/7, MDC 280/28), as well as on the brown ceramic body of samples MDC 282/14 (rim) and MDC 84/4 (core), a weak peak at ca. 670 cm^{-1} was observed along with Raman shifts of hematite (Fig. 9e). This band suggests the presence of magnetite, probably due to an incomplete transformation process of Fe_3O_4 to Fe_2O_3 in an oxidizing atmosphere during cooling (Lofrumento et al., 2004).

The black matrix in cores, however, is characterized by significant differences with respect to the red matrix, highlighting spectral evidence of Fe(II)-rich phases. The most intense bands at ca. 680, 535 and 301 cm^{-1} can be attributed to magnetite (see Fig. 9f above; Shebanova and Lazor, 2003). However, μ-RS is not equally sensitive to all the iron oxides that might be present in fired clays and it shows lower sensitivity to hercynite and maghemite than to hematite and magnetite (Cianchetta et al., 2015b). Nevertheless, a broad and weaker band at ca. 736 cm^{-1} was occasionally observed in some spectra (Fig. 9f); as reported in the literature (Scarpelli et al., 2014; Cianchetta et al., 2015a), this band could be attributed to the vibrational modes of the spinel structure, hercynite, thus supporting the evidence provided by Mössbauer spectroscopy.

In most Raman spectra, peaks of other minerals were detected along with the most intense bands of Fe(III) and Fe(II) phases. In particular, bands of quartz (ca. 460 cm^{-1}), residual clay minerals (ca. 820 cm^{-1}), and anatase (ca. 143 cm^{-1}) have been identified.

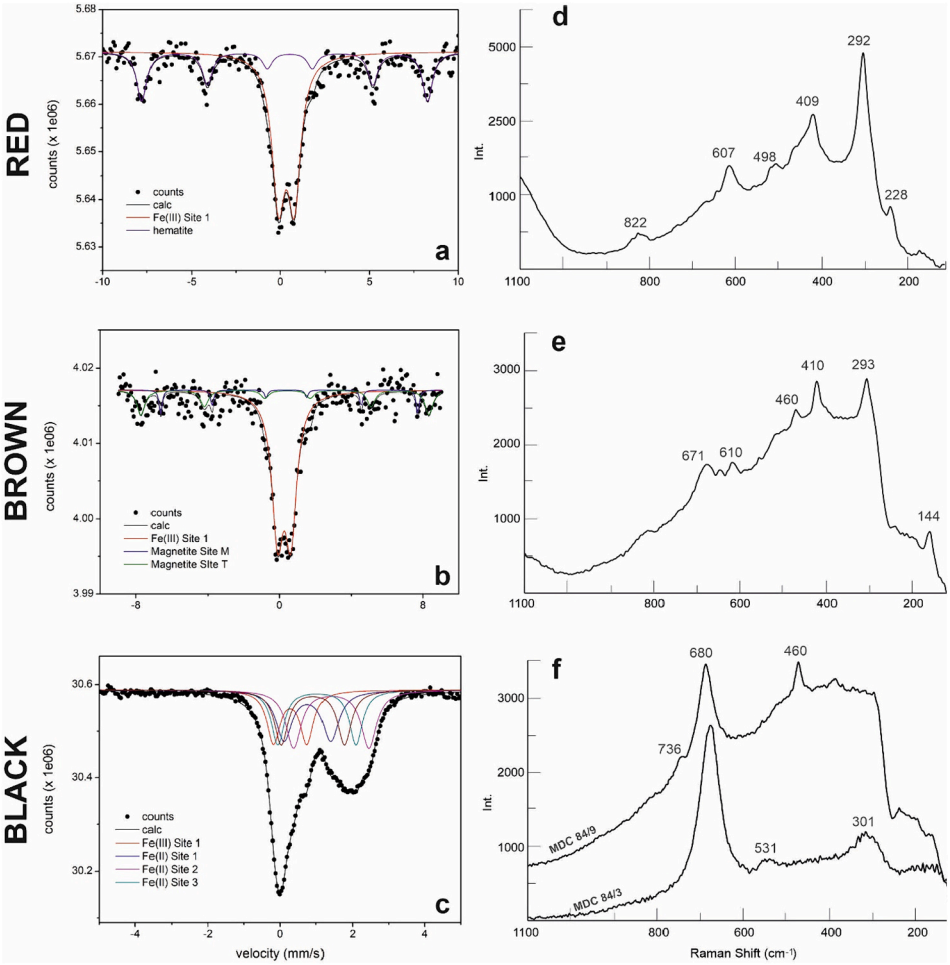

Fig. 9. Mössbauer spectra of red (a), brown (b), and black (c) matrices of the cooking ware and tableware ceramics studied together with their respective Raman spectra (d, e, f). (For interpretation of the references to color in this figure legend, the reader is referred to the web version of this article.)

5. Conclusions

The inclusion of Raman spectroscopy in the characterization of archaeological objects is now a regular practice, and experimental applications straightforwardly demonstrated the reliability of data acquired on complex materials such as the pottery (Bersani et al., 2016).

In this perspective, we tried to address some relevant research queries by comparing bulk analyses with data from μ-RS. Since this technique turned out to be particularly sensitive in the detection of micrometric to sub-micrometric mineral phases, it is fundamental in understanding ceramic manufacturing technologies, from the selection of raw materials to firing conditions in the kiln. In particular, the advantages of μ-RS are:

(1) μ-RS on temper-grains allowed for the identification of mineral solid solutions, like plagioclase and clinopyroxene. The detection of andraditic garnet and forsteritic olivine along with K-feldspar and leucite confirms the source of the volcanic temper to be the Somma-Vesuvius volcanic complex. These μ-RS data are in perfect agreement with the mineral chemistry determined by EDS analyses.

(2) μ-RS can reliably constrain the range of firing temperatures experienced by the pottery, overcoming some problematic issues concerning TiO_2 polymorphs, by investigating the spectral features of ceramic matrices and comparing them with those of ceramic replicas made with LCC fired at a range of carefully controlled temperatures. The expected mineralogical changes of this clay type mainly concern the de-hydroxylation of clay minerals that is characterized by a pronounced decrease of 10 Å dehydroxylated phases' peak intensity in the XRPD patterns; the μ-RS acquisition on archaeological pottery and ceramic replicas highlights comparable behavior of the 730 and 820 cm^{-1} bands that the EFT to be 900–950 °C.

(3) μ-RS turned out to be a valuable tool in determining local redox conditions due to its sensitivity in detecting variations in the oxidation state of iron in Fe(II) and Fe(III) oxides in different parts of the ceramic body which may depend on firing atmosphere. The acquired spectra identify the Fe-bearing phases whose oxidation state determined the color of the pastes: Fe(III) in hematite (α-Fe_2O_3) produced the red color of rims, Fe(II) in magnetite (Fe_3O_4) and hercynite ($FeAl_2O_4$) produced the black color of cores, whereas the coexistence of both Fe(III) and Fe(II) mineral phases resulted in the orange and/or brown color in some portions of the ceramic bodies.

Although hercynite may also be obtained by firing clays rich in organic matter in an oxidizing environment (Maritan et al., 2006), in this case, a non-oxidizing environment with low oxygen fugacity fO_2 was created in the cores, possibly because the time of firing was insufficient to complete oxidation within the interior of the ceramic (Maritan et al., 2006; De Bonis et al., 2017a). Such a condition was also favored by the low interconnection of pores, which hinders the circulation of oxygen in the core of the ceramics (De Bonis et al., 2017a).

(4) The comparison between the results of μ-RS and more traditional techniques (i.e., SEM-EDS, XRPD, Mössabuer spectroscopy) demonstrates a strong correlation between data acquired through the different techniques, confirming the affordability and applicability of μ-RS in the characterization and identification of mineral compositions of the different components of archaeological pottery (and potentially other materials). Finally, μ-RS has obvious advantages over other methods in that small samples are needed (only a thin section is required), the time for sample preparation is minimized, spectral acquisition times are comparatively short, and the method is highly sensitive.

CRediT authorship contribution statement

Chiara Germinario: Writing – review & editing, Writing – original draft, Visualization, Methodology, Investigation, Formal analysis, Conceptualization. **Giuseppe Cultrone:** Writing – review & editing, Resources, Funding acquisition. **Alberto De Bonis:** Writing – review & editing, Visualization, Investigation. **Francesco Izzo:** Writing – review & editing, Investigation. **Alessio Langella:** Writing – review & editing, Resources. **Mariano Mercurio:** Writing – review & editing, Resources. **Luca Nodari:** Writing – review & editing, Investigation. **Christopher R. Vyhnal:** Validation, Writing – review & editing. **Celestino Grifa:** Writing – review & editing, Supervision, Resources, Methodology, Investigation, Funding acquisition, Conceptualization.

Declaration of competing interest

The authors declare that they have no known competing financial interests or personal relationships that could have appeared to influence the work reported in this paper.

Data availability

Data will be made available on request.

Acknowledgements

The authors wish to thank Girolamo Ferdinando De Simone who provided the archaeological samples we investigated within this study. The research was supported by grants from the Department of Science and Technology of the University of Sannio (FRA Grifa) and by the research group RNM179 of the Junta de Andalucia and by Research Project B-RNM-188-UGR20 of the Regional Ministry of University, Research and Innovation of the Junta de Andalucía and FEDER, *a way of making Europe.* The authors extend their sincere thanks to Dr. Branimir Šegvić and an anonymous reviewer who helped us to improve the previous version of the manuscript.

Appendix A. Supplementary data

Supplementary data to this article can be found online at https://doi.org/10.1016/j.clay.2024.107347.

References

Allan, T.E., McMillan, R., 2022. Investigating the application of Raman spectroscopy of carbonaceous material in sedimentary lithic artifacts for archaeological provenancing applications in the Canadian Rockies. Geoarchaeology 37, 450–465. https://doi.org/10.1002/gea.21893.

Aloise, P., Ricca, M., La Russa, M.F., Ruffolo, S.A., Belfiore, C.M., Padeletti, G., Crisci, G. M., 2014. Diagnostic analysis of stone materials from underwater excavations: the case study of the Roman archaeological site of Baia (Naples, Italy). Appl. Phys. A Mater. Sci. Process. 114, 655–662. https://doi.org/10.1007/s00339-013-7890-1.

Alonso-Olazabal, A., Ortega, L.A., Zuluaga, M.C., Alonso-Fernández, C., Jimenez-Echevarría, J., Sarmiento, A., 2022. Glaze characterization of the glazed pottery from the medieval workshop of Vega (Burgos, Spain). J. Raman Spectrosc. 53, 1204–1213. https://doi.org/10.1002/jrs.6328.

Baert, K., Meulebroeck, W., Wouters, H., Cosyns, P., Nys, K., Thienpont, H., Terryn, H., 2011. Using Raman spectroscopy as a tool for the detection of iron in glass. J. Raman Spectrosc. 42, 1789–1795. https://doi.org/10.1002/jrs.2935.

Baert, K., Meulebroeck, W., Ceglia, A., Wouters, H., Cosyns, P., Nys, K., Thienpont, H., Terryn, H., 2012. The potential of Raman spectroscopy in glass studies. In: Proc. SPIE 8422, Integrated Approaches to the Study of Historical Glass, p. 842207. https://doi.org/10.1117/12.981648.

Ballirano, P., De Vito, C., Medeghini, L., Mignardi, S., Ferrini, V., Matthiae, P., Bersani, D., Lottici, P.P., 2014. A combined use of optical microscopy, X-ray powder diffraction and micro-Raman spectroscopy for the characterization of ancient ceramic from Ebla (Syria). Ceram. Int. 40, 16409–16419. https://doi.org/10.1016/j.ceramint.2014.07.149.

Bersani, D., Lottici, P.P., 2016. Raman spectroscopy of minerals and mineral pigments in archaeometry. J. Raman Spectrosc. 47, 499–530. https://doi.org/10.1002/jrs.4914.

Bersani, D., Conti, C., Matousek, P., Pozzi, F., Vandenabeele, P., 2016. Methodological evolutions of Raman spectroscopy in art and archaeology. Anal. Methods 8, 8395–8409. https://doi.org/10.1039/C6AY02327D.

Bikiaris, D., Daniilia, S., Sotiropoulou, S., Katsimbiri, O., Pavlidou, E., Moutsatsou, A.P., Chryssoulakis, Y., 2000. Ochre-differentiation through micro-Raman and micro-FTIR spectroscopies: Application on wall paintings at Meteora and Mount Athos, Greece. Spectrochim. Acta - Part A Mol. Biomol. Spectrosc. 56, 3–18. https://doi.org/10.1016/S1386-1425(99)00134-1.

Bonga, L.A., 2013. Late Neolithic Pottery from Mainland Greece, ca. 5,300-4,300 B.C. Temple University, Philadelphia.

Bongiorno, V., Campodonico, S., Caffara, R., Piccardo, P., Carnasciali, M.M., 2012. Micro-Raman spectroscopy for the characterization of artistic patinas produced on copper-based alloys. J. Raman Spectrosc. 43, 1617–1622. https://doi.org/10.1002/jrs.4167.

Bouchard, M., Smith, D.C., 2003. Catalogue of 45 reference Raman spectra of minerals concerning research in art history or archaeology, especially on corroded metals and coloured glass. Spectrochim. Acta Part A Mol. Biomol. Spectrosc. 59, 2247–2266. https://doi.org/10.1016/S1386-1425(03)00069-6.

Bouzidi, N., Bouzidi, A., Gaudon, P., Merabet, D., Blanchart, P., 2013. Porcelain containing anatase and rutile nanocrystals. Ceram. Int. 39, 489–495. https://doi.org/10.1016/j.ceramint.2012.06.053.

Caggiani, M.C., Cosentino, A., Mangone, A., 2016. Pigments Checker version 3.0, a handy set for conservation scientists: a free online Raman spectra database. Microchem. J. 129, 123–132. https://doi.org/10.1016/j.microc.2016.06.020.

Chiriu, D., Pisu, F.A., Ricci, P.C., Carbonaro, C.M., 2020. Application of Raman Spectroscopy to Ancient Materials: Models and results from Archaeometric analyses. Materials (Basel). https://doi.org/10.3390/ma13112456.

Cianchetta, I., Maish, J., Saunders, D., Walton, M., Mehta, A., Foran, B., Trentelman, K., 2015a. Investigating the firing protocol of Athenian pottery production: a Raman study of replicate and ancient sherds. J. Raman Spectrosc. 46, 996–1002. https://doi.org/10.1002/jrs.4662.

Cianchetta, I., Trentelman, K., Maish, J., Saunders, D., Foran, B., Walton, M., Sciau, P., Wang, T., Pouyet, E., Cotte, M., Meirer, F., Liu, Y., Pianetta, P., Mehta, A., 2015b. Evidence for an unorthodox firing sequence employed by the Berlin Painter: deciphering ancient ceramic firing conditions through high-resolution material characterization and replication. J. Anal. At. Spectrom. 30, 666–676. https://doi.org/10.1039/C4JA00376D.

Colomban, P., 2004. Raman spectrometry, a unique tool to analyze and classify ancient ceramics and glasses. Appl. Phys. A Mater. Sci. Process. 79, 167–170. https://doi.org/10.1007/s00339-004-2512-6.

Colomban, P., 2008. On-site Raman identification and dating of ancient glasses: a review of procedures and tools. J. Cult. Herit. 9, e55–e60. https://doi.org/10.1016/j.culher.2008.06.005.

Colomban, P., Tournie, A., Bellot-Gurlet, L., 2006. Raman identification of glassy silicates used in ceramics, glass and jewellery: a tentative differentiation guide. J. Raman Spectrosc. 37, 841–852. https://doi.org/10.1002/jrs.1515.

Cultrone, G., Rodriguez-Navarro, C., Sebastián, E., Cazalla, O., De La Torre, M.J., 2001. Carbonate and silicate phase reactions during ceramic firing. Eur. J. Mineral. 13, 621–634. https://doi.org/10.1127/0935-1221/2001/0013-0621.

De Bonis, A., Cavassa, L., Grifa, C., Langella, A., Morra, V., 2009. Le ceramiche comuni di Cuma. In: Pasqualini, M. (Ed.), Les Céramiques Communes d'Italie et de Narbonnaise. Actes de La Table Ronde de Naples, Centre Jean Bérard, Napoli, pp. 309–330.

De Bonis, A., Grifa, C., Cultrone, G., De Vita, P., Langella, A., Morra, V., 2013. Raw materials for archaeological pottery from the Campania region of Italy: a petrophysical characterization. Geoarchaeology 28, 478–503. https://doi.org/10.1002/gea.21450.

De Bonis, A., Cultrone, G., Grifa, C., Langella, A., Morra, V., 2014. Clays from the Bay of Naples (Italy): New insight on ancient and traditional ceramics. J. Eur. Ceram. Soc. 34, 3229–3244. https://doi.org/10.1016/j.jeurceramsoc.2014.04.014.

De Bonis, A., Febbraro, S., Germinario, C., Giampaola, D., Grifa, C., Guarino, V., Langella, A., Morra, V., 2016. Distinctive Volcanic Material for the production of Campana A Ware: the Workshop Area of Neapolis at the Duomo Metro Station in Naples, Italy. Geoarchaeology 31, 437–466. https://doi.org/10.1002/gea.21571.

De Bonis, A., Cultrone, G., Grifa, C., Langella, A., Leone, A.P., Mercurio, M., Morra, V., 2017a. Different shades of red: the complexity of mineralogical and physico-chemical factors influencing the colour of ceramics. Ceram. Int. 43, 8065–8074. https://doi.org/10.1016/j.ceramint.2017.03.127.

De Bonis, A., D'Angelo, M., Guarino, V., Massa, S., Anaraki, F.S.F.S., Genito, B., Morra, V., 2017b. Unglazed pottery from the masjed-i jom'e of Isfahan (Iran): technology and provenance. Archaeol. Anthropol. Sci. 9, 617–635. https://doi.org/10.1007/s12520-016-0407-z.

De Simone, G.F., Martucci, C.S., Grifa, C., De Bonis, A., Guarino, V., Morra, V., 2012. Late Antique Connectivity: a Snapshot of Regional Trade in AD 472 Campania. In: SOMA 2012. Identity and Connectivity, Oxford, pp. 971–980.

De Vito, C., Medeghini, L., Mignardi, S., Orlandi, D., Nigro, L., Spagnoli, F., Lottici, P.P., Bersani, D., 2014. Technological fingerprints of Black-Gloss Ware from Motya (Western Sicily, Italy). Appl. Clay Sci. 88–89, 202–213. https://doi.org/10.1016/j.clay.2013.12.026.

Ferrón, C.C., León-Reina, L., Jorge-Villar, S.E., Compaña, J.M., Aranda, M.A.G., Navarrete, J.T.L., Hernández, V., Medianero, F.J., Ramos, J., Weniger, G.-C., Domínguez-Bella, S., Linstaedter, J., Cantalejo, P., de Mar Espejo, M., Valsero, J.J.D., 2014. Combined Raman spectroscopic and Rietveld analyses as a useful and nondestructive approach to studying flint raw materials at prehistoric archaeological sites. Archaeol. Anthropol. Sci. 7, 235–243.

Fintor, K., Gyalai, Z., 2012. Petrographical and micro-Raman analysis of Terra Sigillata shatters from a Vandalic settlement in North-Eastern Hungary. J. Raman Spectrosc. 43, 1796–1804. https://doi.org/10.1002/jrs.4176.

Gardner, E.J., 2003. Technical Analysis of the Ceramics and Appendix 7.1 Graphite Painted Pottery. In: Excavations at Sitagroi, a Prehistoric Village in Northeast Greece: The Final Report, vol. 2. Cotsen Institute of Archaeology, Los Angeles, pp. 283–298.

Gennari, F.C., Pasquevich, D.M., 1999. Enhancing effect of Iron Chlorides on the Anatase-Rutile transition in Titanium Dioxide. J. Am. Ceram. Soc. 82, 1915–1921. https://doi.org/10.1111/j.1151-2916.1999.tb02016.x.

Germinario, C., Cultrone, G., De Bonis, A., Izzo, F., Langella, A., Mercurio, M., Morra, V., Santoriello, A., Siano, S., Grifa, C., 2018a. The combined use of spectroscopic techniques for the characterisation of late Roman common wares from Benevento (Italy). Measurement 114, 515–525. https://doi.org/10.1016/j.measurement.2016.08.005.

Germinario, C., Izzo, F., Mercurio, M., Langella, A., Sali, D., Kakoulli, I., De Bonis, A., Grifa, C., 2018b. Multi-analytical and non-invasive characterization of the polychromy of important archaeological wall paintings at the Domus of Octavius Quartio in Pompeii. Eur. Phys. J. Plus 133, 359. https://doi.org/10.1140/epjp/i2018-12224-6.

Germinario, C., Cultrone, G., Cavassa, L., De Bonis, A., Izzo, F., Langella, A., Mercurio, M., Morra, V., Munzi, P., Grifa, C., 2019. Local production and imitations of late Roman pottery from a well in the Roman necropolis of Cuma in Naples, Italy. Geoarchaeology 34. https://doi.org/10.1002/gea.21703.

Germinario, C., Cultrone, G., De Bonis, A., De Simone, G.F., Gorrasi, M., Izzo, F., Langella, A., Martucci, C.S., Mercurio, M., Morra, V., Vyhnal, C.R., Grifa, C., 2021. Production technology of late Roman decorated tableware from the Vesuvius environs: evidence from Pollena Trocchia (Campania region, Italy). Geoarchaeology 36, 34–53. https://doi.org/10.1002/gea.21819.

Germinario, C., De Bonis, A., Grifa, C., Guarino, V., Marazzi, M., Pepe, C., Rispoli, C., Scotto di Covella, M., Morra, V., 2022. The Mediterranean trading Centre of Vivara (southern Italy): New insights on the production and circulation of pottery during the Bronze Age (16th – 15th century BCE). J. Archaeol. Sci. Rep. 44, 103516 https://doi.org/10.1016/j.jasrep.2022.103516.

Grifa, C., Cultrone, G., Langella, A., Mercurio, M., De Bonis, A., Sebastián, E., Morra, V., 2009. Ceramic replicas of archaeological artefacts in Benevento area (Italy): Petrophysical changes induced by different proportions of clays and temper. Appl. Clay Sci. 46, 231–240. https://doi.org/10.1016/j.clay.2009.08.007.

Grifa, C., De Bonis, A., Langella, A., Mercurio, M., Soricelli, G., Morra, V., 2013. A late Roman ceramic production from Pompeii. J. Archaeol. Sci. 40, 810–826. https://doi.org/10.1016/j.jas.2012.08.043.

Grifa, C., Germinario, C., De Bonis, A., Cavassa, L., Izzo, F., Mercurio, M., Langella, A., Kakoulli, I., Fischer, C., Barra, D., Aiello, G., Soricelli, G., Vyhnal, C.R., Morra, V., 2021a. A pottery workshop in Pompeii unveils new insights on the Roman ceramics crafting tradition and raw materials trade. J. Archaeol. Sci. 126 https://doi.org/10.1016/j.jas.2020.105305.

Grifa, C., Germinario, C., Mercurio, M., Izzo, F., Pepe, F., Bareschino, P., Cucciniello, C., Morra, V., Cultrone, G., Carafa, A., Langella, A., 2021b. Technology, exploitation and consumption of natural resources of traditional brick productions in Madagascar. Constr. Build. Mater. 308, 125022 https://doi.org/10.1016/j.conbuildmat.2021.125022.

Guarino, V., De Bonis, A., Peña, J.T., Verde, M., Morra, V., 2021. Multianalytical investigation of wasters from the Tower 8/Porta di Nola refuse middens in Pompeii: Sr–Nd isotopic, chemical, petrographic, and mineralogical analyses. Geoarchaeology 36, 712–739. https://doi.org/10.1002/gea.21858.

Hein, A., Müller, N.S., Kilikoglou, V., 2009. Great pots on fire: thermal properties of. In: Biró, K.T., Szilágyi, V., Kreiter, A. (Eds.), Vessels: Inside and Outside. Proceedings of the Conference EMAC'07, 9th European Meeting on Ancient Ceramics. Hungarian National Museum, pp. 15–20.

Hernández, V., Jorge-Villar, S., Capel Ferrõn, C., Medianero, F.J., Ramos, J., Weniger, G. C., Domínguez-Bella, S., Linstaedter, J., Cantalejo, P., Espejo, M., Durán Valsero, J.J., 2012. Raman spectroscopy analysis of Palaeolithic industry from Guadalteba terrace river, Campillos (Guadalteba county, Southern of Iberian Peninsula). J. Raman Spectrosc. 43, 1651–1657. https://doi.org/10.1002/jrs.4104.

Huang, E., Chen, C.H., Huang, T., Lin, E.H., Xu, J., 2000. Raman spectroscopic characteristics of Mg-Fe-Ca pyroxenes. Am. Mineral. 85, 473–479. https://doi.org/10.2138/am-2000-0408.

Hunt, A., 2017. The Oxford Handbook of Archaeological Ceramic Analysis. Oxford University Press, Oxford. https://doi.org/10.1093/oxfordhb/9780199681532.001.0001.

Izzo, F., Guarino, V., Ciotola, A., Verde, M., De Bonis, A., Capaldi, C., Morra, V., 2021. An archaeometric investigation in a consumption context: Exotic, imitation and traditional ceramic productions from the Forum of Cumae (southern Italy). J. Archaeol. Sci. Rep. 35 https://doi.org/10.1016/j.jasrep.2020.102768.

Jones, R.E., 1986. Greek and Cypriot Pottery: A Review of Scientific Studies. British School at Athens, Athens.

Jordán, M.M., Boix, A., Sanfeliu, T., de la Fuente, C., 1999. Firing transformations of cretaceous clays used in the manufacturing of ceramic tiles. Appl. Clay Sci. 14, 225–234. https://doi.org/10.1016/S0169-1317(98)00052-0.

Kirmizi, B., Chen, S., Colomban, P., 2019. The Raman signature of protonic species as a potential tool for dating or authentication of glazed pottery. J. Raman Spectrosc. 50, 696–710. https://doi.org/10.1002/jrs.5558.

Kolesov, B.A., Geiger, C.A., 1998. Raman spectra of silicate garnets. Phys. Chem. Miner. 25, 142–151. https://doi.org/10.1007/s002690050097.

Konta, J., 1995. Clay and man: clay raw materials in the service of man. Appl. Clay Sci. 10, 275–335. https://doi.org/10.1016/0169-1317(95)00029-4.

Lafuente, B., Downs, R.T., Yang, H., Stone, N., 2015. The power of databases: The RRUFF project. In: Armbruster, T., Danisi, R.M. (Eds.), Highlights in Mineralogical Crystallography. De Gruyter, pp. 1–30.

Legodi, M.A., de Waal, D., 2007. Raman spectroscopic study of ancient South African domestic clay pottery. Spectrochim. Acta Part A Mol. Biomol. Spectrosc. 66, 135–142. https://doi.org/10.1016/j.saa.2006.02.059.

Locock, A.J., 2008. An Excel spreadsheet to recast analyses of garnet into end-member components, and a synopsis of the crystal chemistry of natural silicate garnets. Comput. Geosci. 34, 1769–1780. https://doi.org/10.1016/j.cageo.2007.12.013.

Lofrumento, C., Zoppi, A., Castellucci, E.M., 2004. Micro-Raman spectroscopy of ancient ceramics: a study of French sigillata wares. J. Raman Spectrosc. 35, 650–655. https://doi.org/10.1002/jrs.1209.

Maniatis, Y., 2009. The emergence of ceramic technology and its evolution as revealed with the use of scientific techniques. In: Shortland, A.J., Freestone, I.C., Rehren, T. (Eds.), From Mine to Microscope: Advances in the Study of Ancient Technology. Oxbow Books, pp. 1–18.

Maniatis, Y., Tite, M.S., 1981. Technological examination of Neolithic-Bronze Age pottery from central and Southeast Europe and from the Near East. J. Archaeol. Sci. 8, 59–76.

Maritan, L., Nodari, L., Mazzoli, C., Milano, A., Russo, U., 2006. Influence of firing conditions on ceramic products: Experimental study on clay rich in organic matter. Appl. Clay Sci. 31, 1–15. https://doi.org/10.1016/j.clay.2005.08.007.

Martina, I., Wiesinger, R., Schreiner, M., 2013. Micro-Raman investigations of early stage silver corrosion products occurring in sulfur containing atmospheres. J. Raman Spectrosc. 44, 770–775. https://doi.org/10.1002/jrs.4276.

Martucci, C.S., Boemio, G., Trojsi, G., De Simone, G.F., 2012. Pollena Trocchia (NA), località Masseria De Carolis. L'analisi dei reperti per la ricostruzione del contesto economico e sociale della villa romana. Amoenitas II, 87–117.

Medeghini, L., Mignardi, S., De Vito, C., Bersani, D., Lottici, P.P., Turetta, M., Costantini, J., Bacchini, E., Sala, M., Nigro, L., 2013. The key role of micro-Raman spectroscopy in the study of ancient pottery: the case of pre-classical Jordanian ceramics from the archaeological site of Khirbet al-Batrawy. Eur. J. Mineral. 25, 881–893. https://doi.org/10.1127/0935-1221/2013/0025-2332.

Medeghini, L., Lottici, P.P., De Vito, C., Mignardi, S., Bersani, D., 2014. Micro-Raman spectroscopy and ancient ceramics: applications and problems. J. Raman Spectrosc. 45, 1244–1250. https://doi.org/10.1002/jrs.4583.

Mercurio, M., Bish, D.L., Cappelletti, P., de' Gennaro, B., de' Gennaro, M., Grifa, C., Izzo, F., Mercurio, V., Morra, V., Langella, A., 2016. The combined use of steam-treated bentonites and natural zeolites in the oenological refining process. Mineral. Mag. 80, 347–362. https://doi.org/10.1180/minmag.2016.080.004.

Montana, G., 2017. Ceramic raw materials. In: Hunt, A. (Ed.), The Oxford Handbook of Archaeological Ceramic Analysis. Oxford University Press, Oxford, pp. 87–100.

Morimoto, N., 1988. Nomenclature of pyroxenes. Mineral. Petrol. 39, 55–76.

Morra, V., De Bonis, A., Grifa, C., Langella, A., Cavassa, L., Piovesan, R., 2013. Minero-petrographic study of cooking ware and pompeian red ware (Rosso Pompeiano) from Cuma (Southern Italy). Archaeometry 55, 852–879. https://doi.org/10.1111/j.1475-4754.2012.00710.x.

Muller, S., Hein, A., Kilikoglou, V., Day, P.M., 2013. Bronze Age cooking pots: thermal properties and cooking methods. Préhistoires Méditerranéennes 4, 1–10.

Nodari, L., Maritan, L., Mazzoli, C., Russo, U., 2004. Sandwich structures in the Etruscan-Padan type pottery. Appl. Clay Sci. 27, 119–128. https://doi.org/10.1016/j.clay.2004.03.003.

Nodari, L., Marcuz, E., Maritan, L., Mazzoli, C., Russo, U., 2007. Hematite nucleation and growth in the firing of carbonate-rich clay for pottery production. J. Eur. Ceram. Soc. 27, 4665–4673. https://doi.org/10.1016/j.jeurceramsoc.2007.03.031.

NORMAL 29/88, 1988. Misura dell'indice di asciugamento (drying index). CNR-ICR, Roma.

NORMAL 7/81, 1981. Assorbimento d'acqua per Immersione Totale - Capacità di Imbibizione. CNR-ICR, Roma.

Olivares, M., Zuluaga, M.C., Ortega, L.A., Murelaga, X., Alonso-Olazabal, A., Urteaga, M., Amundaray, L., Alonso-Martin, I., Etxebarria, N., 2010. Characterisation of fine wall and eggshell Roman pottery by Raman spectroscopy. J. Raman Spectrosc. 41, 1543–1549. https://doi.org/10.1002/jrs.2748.

Ospitali, F., Sabetta, T., Tullini, F., Nannetti, M.C., Di Lonardo, G., 2005. The role of Raman microspectroscopy in the study of black gloss coatings on Roman pottery. J. Raman Spectrosc. 36, 18–23. https://doi.org/10.1002/jrs.1259.

Ospitali, F., Chiavari, C., Martini, C., Bernardi, E., Passarini, F., Robbiola, L., 2012. The characterization of Sn-based corrosion products in ancient bronzes: a Raman approach. J. Raman Spectrosc. 43, 1596–1603. https://doi.org/10.1002/jrs.4037.

Oudbashi, O., Naseri, R., Cultrone, G., Egartner, I., Arizzi, A., 2021. The pottery production from the Deh Dumen Bronze Age graveyard (South-Western Iran): a

chemical, mineralogical and physical study. Herit. Sci. 9, 83. https://doi.org/10.1186/s40494-021-00557-6.
Pinto, J., Prieto, A.C., Coria-Noguera, J.C., Sanz-Minguez, C., Souto, J., 2021. Investigating glass beads and the funerary rituals of ancient Vaccaei culture (S. IV-I BC) by Raman spectroscopy. J. Raman Spectrosc. 52, 170–185. https://doi.org/10.1002/jrs.6049.
Puchowicz, D., Cieslak, M., 2022. Raman Spectroscopy in the Analysis of Textile Structures. In: Pathak, C.S., Kumar, S. (Eds.), Recent Developments in Atomic Force Microscopy and Raman Spectroscopy for Materials Characterization. IntechOpen, Rijeka, pp. 157–177. https://doi.org/10.5772/intechopen.99731.
Redi, D., Cannatelli, C., Esposito, R., Lima, A., Petrosino, P., De Vivo, B., 2017. Somma-Vesuvius' activity: a mineral chemistry database. Mineral. Petrol. 111, 43–67. https://doi.org/10.1007/s00710-016-0462-2.
Retko, K., Legan, L., Ropret, P., 2021. SERS procedure using photoreduced substrates and reflection FTIR spectroscopy for the study of natural organic colourants. J. Raman Spectrosc. 52, 130–144. https://doi.org/10.1002/jrs.6035.
RILEM 1980, 1980. Recommended tests to measure the deterioration of stone and to assess the effectiveness of treatment methods. In: Commission 25 - PEM: Protection et Erosion des Monuments.
Rygula, A., Klisińska-Kopacz, A., Krupska, P., Kuraś, E., del Hoyo-Meléndez, J.M., 2021. The surface degradation of Baltic amber: the depth-profiling analysis and its application to historical object. J. Raman Spectrosc. 52, 123–129. https://doi.org/10.1002/jrs.5942.
Santacroce, R., Cioni, R., Marianelli, P., Sbrana, A., Sulpizio, R., Zanchetta, G., Donahue, D.J., Joron, J.L., 2008. Age and whole rock–glass compositions of proximal pyroclastics from the major explosive eruptions of Somma-Vesuvius: a review as a tool for distal tephrostratigraphy. J. Volcanol. Geotherm. Res. 177, 1–18.
Scarpelli, R., Clark, R.J.H., De Francesco, A.M., 2014. Archaeometric study of black-coated pottery from Pompeii by different analytical techniques. Spectrochim. Acta Part A Mol. Biomol. Spectrosc. 120, 60–66. https://doi.org/10.1016/j.saa.2013.09.139.
Shebanova, O.N., Lazor, P., 2003. Raman spectroscopic study of magnetite (FeFe2O4): a new assignment for the vibrational spectrum. J. Solid State Chem. 174, 424–430. https://doi.org/10.1016/S0022-4596(03)00294-9.
Short, L., Thoms, A.V., Cao, B., Sinyukov, A.M., Joshi, A., Scully, R., Sanders, V., Voronine, D.V., 2015. Facile residue analysis of recent and prehistoric cook stones using handheld Raman spectrometry. J. Raman Spectrosc. 46, 126–132. https://doi.org/10.1002/jrs.4593.
Shoval, S., Boudeulle, M., Panczer, G., 2011a. Identification of the thermal phases in firing of kaolinite to mullite by using micro-Raman spectroscopy and curve-fitting. Opt. Mater. (Amst). 34, 404–409. https://doi.org/10.1016/j.optmat.2011.08.031.
Shoval, S., Yadin, E., Panczer, G., 2011b. Analysis of thermal phases in calcareous Iron Age pottery using FT-IR and Raman spectroscopy. J. Therm. Anal. Calorim. 104, 515–525. https://doi.org/10.1007/s10973-011-1518-5.
Singha, M., Singh, L., 2016. Vibrational spectroscopic study of muscovite and biotite layered phyllosilicates. Indian J. Pure Appl. Phys. 54, 116–122.
Smith, G.D., Clark, R.J.H., 2004. Raman microscopy in archaeological science. J. Archaeol. Sci. 31, 1137–1160. https://doi.org/10.1016/j.jas.2004.02.008.
Tite, M.S., 2008. Ceramic production, provenance and use—a review. Archaeometry 50, 216–231. https://doi.org/10.1111/j.1475-4754.2008.00391.x.
Tite, M.S., Kilikoglou, V., Vekinis, G., 2001. Strength, toughness and thermal shock resistance of ancient ceramics, and their influence on technological choice. Archaeometry 43, 301–324. https://doi.org/10.1111/1475-4754.00019.
Tomasini, E.P., Halac, E.B., Reinoso, M., Di Liscia, E.J., Maier, M.S., 2012. Micro-Raman spectroscopy of carbon-based black pigments. J. Raman Spectrosc. 43, 1671–1675.
Vandenabeele, P., Van Pevenage, J., 2016. Raman Spectroscopy and the Study of Ceramic Manufacture: Possibilities, Results, and Challenges. Oxford Handb. Archaeol. Ceram. Anal. https://doi.org/10.1093/oxfordhb/9780199681532.013.29
Verde, M., De Bonis, A., D'Uva, F., Guarino, V., Izzo, F., Rispoli, C., Borriello, G., Giglio, M., Iavarone, S., Morra, V., 2022. Minero-petrographic investigation on Roman pottery found in a dump in the workshop area of Cumae (southern Italy). J. Archaeol. Sci. Rep. 42, 103376.
Wang, A., Jolliff, B.L., Haskin, L.A., Kuebler, K.E., Viskupic, K.M., 2001. Characterization and comparison of structural and compositional features of planetary quadrilateral pyroxenes by Raman spectroscopy. Am. Mineral. 86, 790–806. https://doi.org/10.2138/am-2001-0703.
Wang, A., Kuebler, K.E., Jolliff, B.L., Haskin, L.A., 2004. Raman spectroscopy of Fe-Ti-Cr-oxides, case study: Martian meteorite EETA79001. Am. Mineral. 89, 665–680.
Whitney, D.L., Evans, B.W., 2010. Abbreviations for names of rock-forming minerals. Am. Mineral. 95, 185–187. https://doi.org/10.2138/am.2010.3371.
Zoppi, A., Lofrumento, C., Castellucci, E.M., Sciau, P., 2008. Al-for-Fe substitution in hematite: the effect of low Al concentrations in the Raman spectrum of Fe2O3. J. Raman Spectrosc. 39, 40–46. https://doi.org/10.1002/jrs.1811.